Ultra-stable radioactive microspheres enabled by radiation-induced graft polymerization for imaging-guided intra-arterial brachytherapy

Xiao Xu

Shanghai Institute of Applied Physics

Hu Chen

Xiamen University

Yangjie Wang

Shanghai Institute of Applied Physics

Pan He

Affiliated Hospital of Southwest Medical University

Zhenwen Zhao

Xiamen University

Hongwei Cheng

Xiamen University   https://orcid.org/0000-0002-4251-0645

Xing Gao

Xiamen University

Yesi Shi

Xiamen University

Yesen Li

The First Affiliated Hospital of Xiamen University

Jinxiong Huang

The First Affiliated Hospital of Xiamen University

Yisheng Peng

Xiamen University

Cheng-Chao Chu

Xiamen Univesity

Yang Zhang

Xiamen University

Chao Liu

Xiamen University

Bo Li

Affiliated Hospital of Southwest Medical University

Jingsong Mao

First Hospital of China Medical University

Hongjuan Ma

Shanghai University   https://orcid.org/0000-0001-8160-7194

Gang Liu (✉ gangliu.cmitm@xmu.edu.cn)

Xiamen University   https://orcid.org/0000-0003-2613-7286

Article

Keywords:

Additional Declarations: There is **NO** Competing Interest.

Ultra-stable radioactive microspheres enabled by radiation-induced graft polymerization for imaging-guided intra-arterial brachytherapy

Xiao Xu[1,2#], Hu Chen[1,#], Yangjie Wang[3], Pan He[1], Zhenwen Zhao[1], Hongwei Cheng[1], Xing Gao[1], Yesi Shi[1], Yesen Li[4], Jinxiong Huang[4], Yisheng Peng[1], Chengchao Chu[1], Yang Zhang[1], Chao Liu[1], Bo Li[5], Jingsong Mao[1,*], Hongjuan Ma[2,*], and Gang Liu[1,*]

[1] State Key Laboratory of Molecular Vaccinology and Molecular Diagnostics, Center for Molecular Imaging and Translational Medicine, School of Public Health, Xiamen University, 361102 Xiamen, China.

[2] Shanghai Applied Radiation Institute, Shanghai University, Shanghai 200444, China.

[3] Shanghai Institute of Applied Physics, Chinese Academy of Sciences, Shanghai 201800, China.

[4] Department of Nuclear Medicine, The First Affiliated Hospital of Xiamen University, School of Medicine, Xiamen University, Xiamen 361003, China.

[5] Department of General Surgery (Hepatobiliary Surgery), The Affiliated Hospital of Southwest Medical University, Luzhou 646000, China.

Abstract

Intravascular brachytherapy requires advances in radio-embolization technologies that combine brilliant radiostability efficacy with a facile and green synthesis route. We report a hybrid-integrated radioactive microsphere strategy using phosphorylcholine-modified lutetium-177 coordinated polymeric microspheres (^{177}Lu-PCMs) that were fabricated via radiation-induced graft polymerization for imaging-guided locoregional intravascular brachytherapy. The underlying formation mechanism of ^{177}Lu-PCMs is elucidated using first-principles computations and density functional theory calculations and ^{177}Lu loading mechanisms was investigated with Near-edge and extended X-ray absorption fine structure spectroscopy. The engineered ^{177}Lu-PCMs exhibit excellent mechanical properties, good hydrophilicity, and controlled sphere

diameter. These features provide advantages of ultra-stable and ultra-selective embolic radio-theranostics, which is demonstrated in different preclinical rodent models and isolated human liver tumor tissues. During locoregional intra-arterial brachytherapy, ^{177}Lu-PCMs can be visualized *via* SPECT to validate the *in vivo* biodistribution and retention in real time, achieving precise delivery, effective anti-cancer treatment, and a distinguished safety profile without degradation, ectopic embolization, and adverse reactions. Therefore, this study may offer a new avenue for the development of a highly innovative and translational approach for precision intravascular brachytherapy.

Introduction

Intra-arterial brachytherapy (IAB) or transarterial radioembolization (TARE) using radioactive microspheres is a promising form of intravascular brachytherapy for malignant solid tumors[1, 2]. The goal of IAB is to deliver a high dose of radionuclides into the tumors while avoiding radiation damage to the surrounding normal tissues. Thus, the design and development of excellent radionuclide carriers is essential in the administration of IAB. In this context, it is crucial to prevent radiological diseases caused by ectopic embolism of radiopharmaceuticals and off-targeting of nuclides (*i.e.*, radionuclide leaching and extrahepatic shunting), as well as the waste of drugs due to blocked microcatheters and possible public health safety issues due to additional radiation.

In one example, ^{90}Y glass microspheres produced by neutron activation often contain unwanted radioisotopes with long half-life (e.g., glass microspheres have impurities such as alumina and silica)[3]. [90]Y is not suitable for biomedical imaging, and conventional ^{99m}Tc-macroaggregated albumin (^{99m}Tc-MAA) poorly predicts the intrahepatic distribution of ^{90}Y microspheres in hepatic radioembolization[4]. The radionuclide is another key component in intravascular brachytherapy. [177]Lu is an attractive radionuclide for both diagnostic and therapeutic applications due to its good radiochemical properties. [177]Lu is a trivalent lanthanide metal that can be readily bound to various compounds with high radiolabeling yields[5, 6]. [177]Lu is capable of emitting low-energy gamma (γ) rays, allowing scintigraphy and dosimetry using the same therapeutic compound[7, 8, 9]. The beta particles from ^{177}Lu have a half-life of 6.7 days. With a longer half-life and differences in energy spectra, less activity is needed when

using ^{177}Lu to attain the same radiation-absorbed dose compared to ^{90}Y or ^{166}Ho, making it suitable for transport and clinical applications.

With inspiration from the "the holy grails of chemistry" in combination with "green chemistry," we hypothesized that ultra-stable and ultra-selective ^{177}Lu coordinated microspheres could be fabricated via radiation-induced graft polymerization (RIGP) for single-photon emission computed tomography (SPECT) image-guided locoregional IAB. We report a new type of multi-functional phosphorylcholine-modified ^{177}Lu coordinated polymeric microspheres (^{177}Lu-PCMs). The phosphorylcholine-modified coordination polymeric microspheres (PCMs) were fabricated via two-step polymerization involving emulsion suspension polymerization (ESP) for poly(ethenylbenzene) microspheres (PEBMs) and ^{60}Co RIGP of 2-methacryloyloxy ethyl phosphorylcholine (MPC) monomers to obtain PCMs. ^{177}Lu coordinates with PCMs in an O,O-bidentate chelating configuration for safe and stable IAB and SPECT imaging-guide diagnosis as a noninvasive way to track the ^{177}Lu-PCMs *in vivo* (Scheme 1). 2-methacryloyloxy ethyl phosphorylcholine (MPC) monomers are modified with PEBMs by covalent bonding to obtain functional groups capable of binding ^{177}Lu with hydration layer synergy and no binding space for long half-life radioisotope impurities, which are often produced in neutron reactors. ^{177}Lu-PCMs featuring optimal density, strong hydrophilicity, good dispersibility in aqueous solution and their physicochemical stability allow more uniform distribution in the vascular bed of tumors without systemic toxicity to major organs, which is demonstrated in rats, rabbits, and pigs models. Most importantly, ^{177}Lu-PCMs show significant antitumor efficiency in different preclinical rodent models and isolated human liver tumor tissues. Our results show that the ^{177}Lu-PCMs could be used as cancer embolic theranostics for precision IAB and have high potential for clinical translation.

1
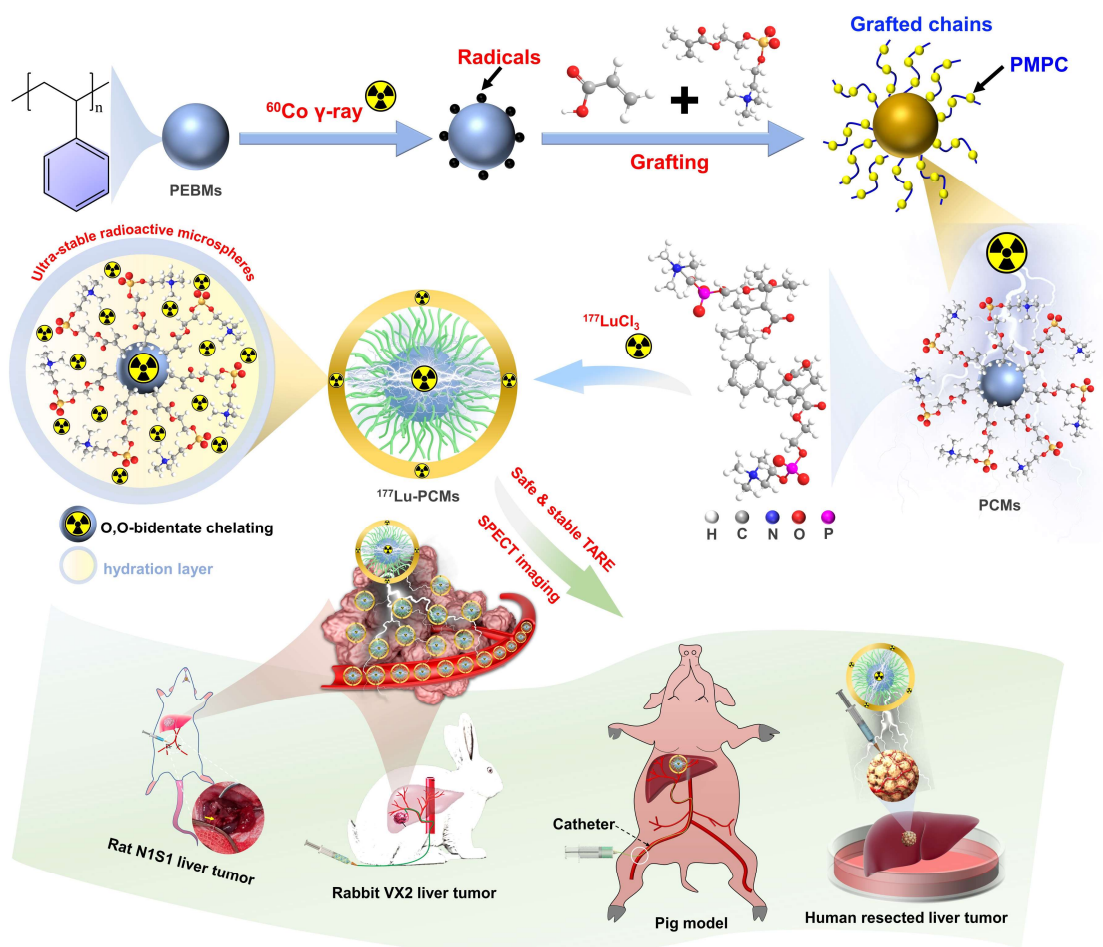
Scheme 1. Schematic illustration of the strategy for large-scale fabrication of ^{177}Lu coordinated phosphorylcholine-modified polymeric microspheres by a novel ESP-RIGP technology. The ^{177}Lu loading mechanisms involve the formation of a stable complex *via* three phosphorylcholines in a cooperative ligand complexation with hydration layer synergy. These features synergistically enhance the radioactive stability of ^{177}Lu-PCMs based on hydrogen bonding-mediated hydration layer. ^{177}Lu-PCMs display high radiostability, excellent mechanical properties, good hydrophilicity, and controlled sphere size, which could meet the needs of clinical precision intravascular brachytherapy. The safety and theranostic efficacy of ^{177}Lu-PCMs as an ultra-stable and ultra-selective embolic agent for intra-arterial brachytherapy are demonstrated in a rat N1S1 model, rabbit VX2 liver tumor model, pig model, and isolated human hepatocellular carcinoma tissues.

Results

Syntheses and characterizations of PCMs, and ^{177}Lu-PCMs. PCMs were fabricated via a novel technique of two-step polymerization involving the ESP of ethenylbenzene

(EB) (Supplementary Fig. 1a) and ^{60}Co RIGP of MPC and acrylic acid (AA) (Scheme 1). The ESP process was highly controllable, and well-dispersed microspheres were obtained via control of the corresponding reaction conditions, such as the reaction temperature and stirring rate. The microspheres featured good sphericity, controlled spheres diameter, and narrow diameter distributions (Supplementary Fig. 2). Notably, the microspheres were synthesized at the kilogram scale in the laboratory (Supplementary Fig. 1b). RIGP technique can be used for grafting polymerization functional monomers on the surface or inside of the material by activate the hydrocarbon bonds of substances at room temperature or even lower temperature, and without adding chemical additives, such as metal catalysts[10]. Meanwhile, [60]Co γ-ray irradiation is widely used for sterilization, which depicts another advantage of material preparation especially for application in clinical medicine[11]. Next, ^{177}Lu was chelated with PCMs in an O,O-bidentate chelating configuration under ultrasonic heating conditions to obtain ^{177}Lu-PCMs.

Fourier transform infrared spectrometry (FT-IR) and X-ray photoelectron spectroscopy (XPS) were employed to characterize the chemical structures of the PEBMs and PCMs. For pristine PEBMs (Fig. 1a), the characteristic peaks observed at 3024.23 and 3062.81 cm^{-1} and those at 2923.07 and 2852.34 cm^{-1} are assigned as aromatic and aliphatic C-H stretching vibrations, respectively. The narrow bands at 698.80 cm^{-1} and 756.07 cm^{-1} are assigned to out-of-plane bending vibration of the C-H bond of PEBMs, and the characteristic peaks at 1449.52, 1493.52, and 1600.33 cm^{-1} correspond to the C=C stretching vibration of the benzene ring. In the range of 1702.75-1996.86 cm^{-1}, there are also some serrated absorption peaks due to the vibrations of the mono-substituted benzene ring. Compared with the PEBM spectra, the absorbance intensity of aromatic and aliphatic C-H in the PCM spectra was significantly decreased, showing that [60]Co γ-ray breaks the abundant C-H bonds on the outermost surface of PEBMs. This provides a high density of reactive sites (free radicals) and triggers graft polymerization reaction without affecting the intrinsic properties of the substrate material[12]. New stretching vibrations of P=O, P-O, and C=O occurred at 1241.12, 964.56, and 1720.31 cm^{-1}, respectively[13], indicating that MPC was successfully grafted

1   onto the trunk PEBMs (Fig. 1a and Supplementary Fig. 3a).

2   Compared with the XPS spectra of PEBMs, the XPS spectra of PCMs show unique

3   P 2p peaks of P on the phosphorylcholine-modified outer surface of PCMs (Fig. 1b).

4   The high-resolution spectra of P $2p_{3/2}$ and P $2p_{1/2}$ confirmed that the MPC monomer

5   was successfully grafted onto the PEBMs (Supplementary Fig. 3b and Supplementary

6   Table S1). Furthermore, the observed high-resolution XPS spectra of O 1s for PCMs

7   were simulated using two-component Gaussian-Lorentzian sum functions. As shown in

8   Fig. 1c, the O 1s spectrum of PCMs can be separated into two peaks at 532.13 and

9   532.94 eV, which correspond to the oxygen of the P=O species and the P-O species in

10   the phosphorylcholine group, respectively. This further illustrates that the PCMs were

11   successfully synthesized. The crystal structures of the microspheres before and after

12   modification were analyzed by X-ray diffraction (XRD). One characteristic diffraction

13   peak for the crystalline structure of typical PEBMs was observed at 19.2° in all the

14   obtained spectra. This suggests that the crystal structure was well maintained after the

15   ^{60}Co γ-ray RIGP modification (Supplementary Fig. 3c).

16   It is well known that hydrated electrons, ·OH radicals, and H_3O^+ ions are the major

17   molecular species produced as a series of free radicals via ^{60}Co γ-ray irradiation[14]. We

18   believe that first-principles density functional theory (DFT) calculations for the RIGP

19   reaction can guide the design of next-generation radioactive microsphere precursors.

20   The first-principles DFT computations were performed on the reaction pathways of

21   RIGP (Fig. 1d, e). As expected, these reaction pathways and energy profiles support the

22   fact that the reaction was dehydrogenated during both ^{60}Co γ-ray radiation-induced

23   breaks of the aliphatic C-H bonds (Supplementary Fig. 4a) and aromatic C-H bonds

24   (Supplementary Fig. 4b). The reactants of these two reactions are the same, the energies

25   of the corresponding transition states (TS) are 0.47 eV and 0.50 eV, respectively, and

26   their transition state energy differences are 0.03 eV. The results indicated that C-H bond

27   breakage on the aliphatic group of the ^{60}Co γ-ray-induced reactants is more likely to

28   occur than that on the benzene ring, and more ^{60}Co γ-ray-initiated C-H bond breakage

29   on the aliphatic group of the reactants will result in more products generated. The

30   transition state energy of the RIGP reaction on the aliphatic C-H bond (6.45 eV) is

larger than that of the RIGP reaction on the benzene ring C-H bond (0.77 eV). However, more products are generated due to the ^{60}Co γ-ray-induced C-H bond breakage on the reactant aliphatic group. Thus, compared to the RIGP reaction on the benzene ring C-H bond, the RIGP reaction on the reactant aliphatic C-H bond is the predominant reaction for the RIGP reaction. The benzene ring in the aromatic group consists of conjugated non-deterministic π-bonds, which probably results in the energy absorbed by the benzene ring being rapidly redistributed throughout the benzene ring when irradiated with ^{60}Co γ-rays. The conjugated structure formed by six π-electrons makes the γ photon collision-induced attenuation more efficient. The energy barriers between the reactants and TS were noted to be 8.18 eV and 1.09 eV during RIGP, which implies that they are heat-absorbing (ΔE = 0.65 eV) (Fig. 1d) and exothermic (ΔE = -0.82 eV) (Fig. 1e), respectively.

Scanning electron microscopy (SEM) results show that the PEBMs consist of well-dispersed microspheres with an average diameter of 42.1 μm was obtained by *ImageJ* software analysis (Supplementary Fig. 2a). The particle size of PEBMs can be adjusted by changing the preparation conditions to satisfy the requirements. The surface of the PCMs does not show any obvious change after RIGP (Fig. 1f). Lognormal differential distributions of particle sizes were weighted by volume for the analysis of PCMs in deionized water, which showed that the mean hydrodynamic diameter was 42.2 μm (Supplementary Fig. 3d). Furthermore, compared with the energy dispersion spectroscopy (EDS) mapping of PEBMs (Supplementary Fig. 5a), EDS mapping of C, O, N, and P showed that phosphorylcholine groups were widely distributed on the entire surface of the PCMs (Supplementary Fig. 5b). We chose PCMs with an average diameter of 42.2 μm in this study for animal embolization because this value is consistent with the requirements of radioactive microspheres for intravascular brachytherapy. The densities of the PCMs (1.11 g/mL) were very close to that of blood (1.05 g/mL), indicating PCMs can be more uniformly distributed within the blood stream. Therefore, they could potentially be more uniformly distributed throughout a tumor's vascular bed than glass microspheres whose density are twice as much as PCMs.

The PCMs must have strong mechanical properties to maintain sphericity within the

tumor vasculature and prevent fragmentation in the tumor's vascular bed. The 2D and 3D AFM image of PEBMs and PCMs show good sphericity and stable microscopic morphology (Supplementary Fig. 6a and 6c). The PEBMs had an average Young's modulus of 385 GPa, and that of PCMs was 197 GPa (Supplementary Fig. 6b and 6d). The results show that the mechanical properties of the microspheres were well maintained during preparation process, which is beneficial for use in intra-arterial brachytherapy.

Due to the smooth and dense structure of the surface of the PEBM microspheres prepared by the ESP technique, such a structure is more conducive to the chemical and biological activation of the surface groups and the reduction of non-specific adsorption. Supplementary Fig. 7a and its inset show the N_2 sorption isotherms and pore diameter distribution curves of PCMs. The Brunauer-Emmet-Teller (BET) surface area of PCMs was 1.5 m^2/g, which is far higher than that of the PEBMs (Supplementary Fig. 7b). PCMs showed a porous structure with a total pore volume of 2.6 mm^3/g. This can be regulated to control the polymer chain conformation and resulting nanopore structure by changing the dose absorbed by the PEBMs, which represents the number of active sites for RIGP.

Hydrophilicity is another important factor that influences the adsorption performance and reaching the distal end vessels of radioactive microspheres[15]. Supplementary Fig. 8a and b show representative photographs of the water contact angle tests at 0, 0.1, and 0.5 s after the contact of a water drop with the PEBMs and PCMs. Compared with the contact angle of PEBMs (130.2°, t=0.5 s), the water drop spreads out on the PCMs' surface within 0.5 s of contact, and the corresponding contact angle was 46.5°. The significant decrease in contact angle indicates great improvement of the hydrophilic property of PCMs compared with PEBMs, and the strong hydrophilicity and slipperiness of PCMs significantly boost their adsorption efficiency for metal nuclides and enable them to pass through Teflon-based microcatheters without blocking the catheter lumen.

Radiolabeling efficiency, radiostability, and SPECT imaging of ^{177}Lu-PCMs. The

1   radiolabeling efficiency was tested by thin-layer chromatography (TLC) and the [177]Lu-

2   PCMs showed a relatively high result (higher than 97%) (Supplementary Fig. 9a). To

3   verify the imaging capability of ^{177}Lu-PCMs, we performed SPECT imaging on them

4   with radioactivity ranging from 7.4 to 37 MBq and free [177]LuCl$_3$. We then circled the

5   results of imaging to extract the signal intensity versus radioactivity in the images at

6   different doses for linear analysis. The SPECT signal intensity increased linearly with

7   the radioactivity of microspheres (Supplementary Fig. 9b).

8   As expected, ^{177}Lu in the ^{177}Lu-PCMs can be stably bound to the PCMs and was

9   observed at the bottom of a test tube when the microspheres settled under SPECT

10   scanning (Fig. 1g, h,). The amount of free ^{177}Lu that was shed from the ^{177}Lu-PCMs

11   was also investigated using radioactivity counting in saline and human serum. The

12   radiostability results showed that ^{177}Lu-PCMs were very stable in both cases, and less

13   than 12% free ^{177}Lu was shed even after 240 h (Supplementary Fig. 9c).

14
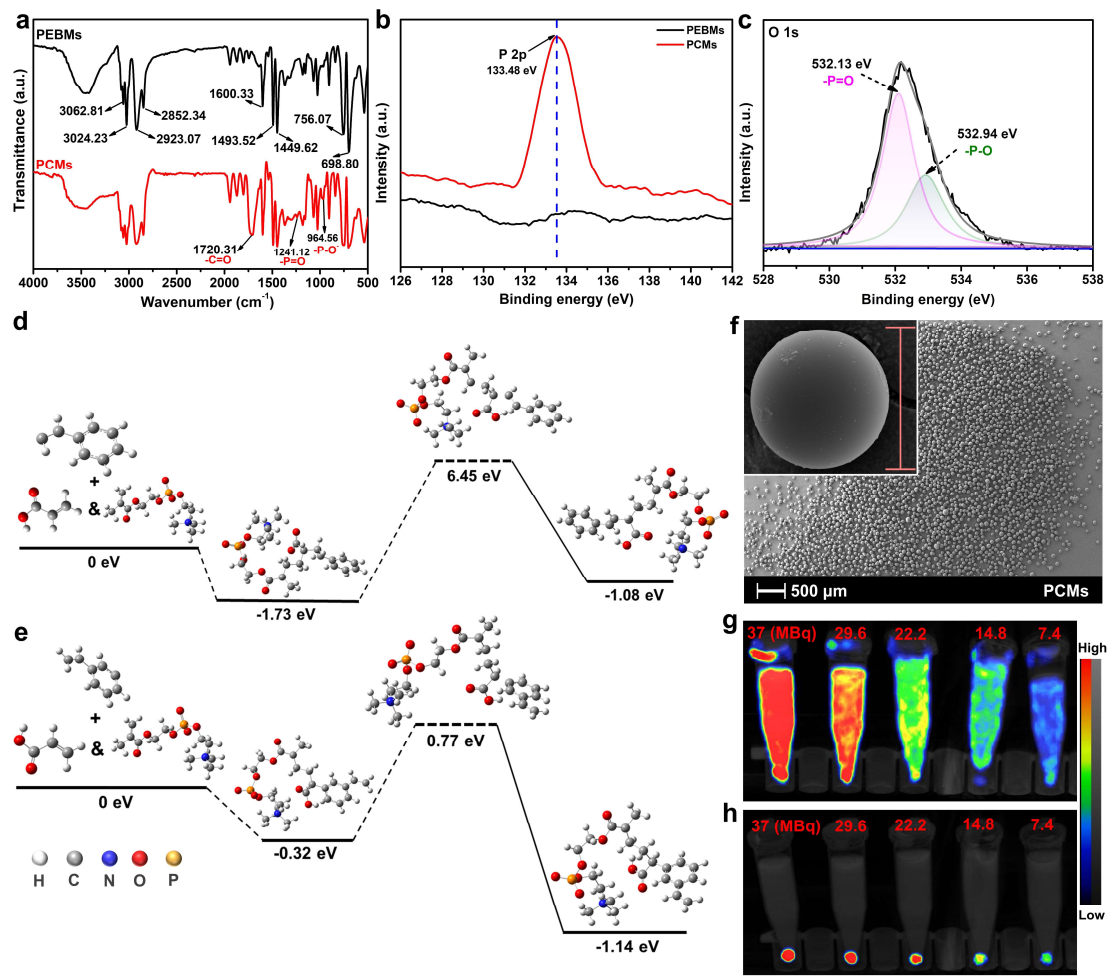
15   **Fig. 1** Physiochemical characterization and RIGP reaction pathway analysis. **a** FT-IR

9

spectra of PEBMs and PCMs. **b** XPS spectra of PEBMs and PCMs. **c** High-resolution XPS spectra of PCMs, focusing on the O 1s peak in the binding energy range of 528–538 eV. Energy profiles of the reaction path: RIGP reaction on (**d**) aliphatic C-H bonds and (**e**) aromatic C-H bonds. The horizontal dashed lines represent transition states, and the relative energies (ΔE, eV) are denoted in black text. **f** Scanning electron microscopy images of PCMs, showing a monodisperse micron-sized microsphere with good sphericity. Three-dimensional (3D) SPECT/CT images of ^{177}LuCl$_3$ (**g**) and ^{177}Lu-PCMs (**h**) dispersed in saline with radioactivity ranging from 7.4 to 37 MBq.

Coordination mechanism of PCMs with Lu-PCMs. Lu-PCMs maintained an integrated structure with Lu binding (Supplementary Fig. 10a), and EDS mapping of the Lu-PCMs showed a uniform distribution of Lu on the surfaces (Supplementary Fig. 10b). The XPS profile of the Lu-PCMs displays two new Lu 4d peaks at 198.95 eV and 208.13 eV, which are assigned to Lu 4d$_{5/2}$ and Lu 4d$_{3/2}$, respectively. These suggest that the valence of bound Lu was not changed (Supplementary Fig. 10c, Table S1). Furthermore, in the case of Lu-PCMs, the relative intensity of P=O greatly decreased, and the position of P=O and P-O was shifted to lower binding energy, indicating increased electron density for the oxygen atoms. This demonstrated that the Lu mainly interacted with not only P=O, but also P-O of the phosphorylcholine group (Fig. 1c and Supplementary Fig. 10d), leading to the effective binding of Lu by the fabricated PCMs.

The oxygen *K*-edge NEXAFS spectra of the PCMs and Lu-PCMs are shown in Supplementary Fig. 11a. The peaks and the shoulder structures in the PCMs were observed at 533.6 eV, 540.1 eV, and 544.8 eV. After binding Lu, the characteristic absorption shoulder peak at 544.8 eV disappeared, and a new broad peak appeared at 538.8-540.8 eV. The energy positions of the new peak can be speculated to correspond to the transitions of O1s(P=O)→π^*(P=O), O1s→σ^*(O-P), and O1s→σ^*(P=O). Each peak intensity was reduced when the binding reaction between the PCMs and the Lu was promoted. Therefore, we propose that the PCMs bound the Lu at the oxygen atoms of P=O and P-O bonds. Considering the double bonds of the PCMs, it is possible that the oxygen atoms of the P=O of the PCMs interact with the Lu. This result corresponds

1   with the results for XPS.

2   The coordination environment of the trivalent Lu ions with PCMs was studied using

3   extended X-ray absorption fine structure (EXAFS) spectra, which provide information

4   about the interatomic interactions between Lu and the phosphorylcholine ligands. The

5   behavior of the ligands has practical importance in metal nuclide labeling processes that

6   are used on an industrial scale. The X-ray Absorption Near Edge Structure (XANES)

7   spectrum of the Lu-PCMs (Fig. 2a) showed general agreement with previously

8   published results on the shape, intensity, and energy[16]. The Lu absorption edge of Lu-

9   PCMs was found at 9250.54 eV, and the maximum energy was 9282.61 eV, which

10   suggests the adsorption of Lu onto the PCMs. Furthermore, the EXAFS wavelet

11   transform plot (Fig. 2b) of Lu-PCMs showed only one high intensity centered around k

12   =4.0 Å^{-1} and R =1.8 Å, corresponding to Lu−O coordination. Next, quantitative

13   EXAFS fitting was conducted to extract the structural parameters and obtain the precise

14   coordination configuration of Lu in Lu-PCMs. The EXAFS analysis indicated that there

15   are two types of Lu-O coordination shells around the Lu in the Lu-PCMs, including

16   distances of 2.2 Å and 2.36 Å (Fig. 2c and 2d, Supplementary Fig. 11b, Table S2). The

17   coordination environment of Lu consists of 5.9 ± 1.5 light-scattering oxygen atoms (Lu-

18   O=P-) on the first shell, which are attributed to the oxygen coordinated with the Lu,

19   while the additional 5.9 ± 1.5 light-scattering oxygen atoms of -P-O- on the second

20   shell are the oxygen close to the Lu. These abundant coordinated oxygen atoms of

21   P=O/P-O- give the PCMs high binding affinity to the Lu.

22   DFT calculation of the Lu-bound PCMs shows that the coordination mechanism fits

23   well with the result of the EXAFS analysis. The enthalpies (ΔH) and Gibbs free energies

24   (ΔG) were obtained via DFT calculation and indicated a six-coordinate 3:1 Lu complex

25   with mixed coordination of the three ligands for Configuration A and Configuration B.

26   Binding energy studies revealed that the chelating configuration B is the most stable

27   one (Fig. 2e). The coordination environment generated from the DFT calculation agrees

28   with the experimental EXFAS results (Fig. 2e and Supplementary Fig. 12).

29   An independent gradient model based on Hirshfeld partition (IGMH) was employed

30   to analyze the interaction strength of ligand molecules of configuration B with Lu[17]. As

1　shown in Fig. 2f, all the intermolecular interactions from the IGMH maps revealed that

2　the δg^{inter} values of the Lu-O bond (chelating configuration B) range from -0.82 to -

3　1.36 eV. This indicates that the phosphorylcholine has strong chemical bonding with

4　Lu.

5　　We combined IGMH analysis and the bond critical point (BCP) in atoms-in-

6　molecules theory to quantitatively study the strength of the Lu-O bond[17]. The BCP and

7　bond paths between Lu and choline phosphate were generated by Multiwfn. The

8　isosurface of δg^{inter} defined by IGMH clearly shows the interaction between Lu and all

9　six surrounding oxygen atoms, and the light blue regions on the isosurface indicate that

10　the electron density in these regions is larger than in the normal dispersive interaction

11　regions. The IGMH maps also show the electron density values of the BCP

12　corresponding to these interactions, and the shorter the Lu-O bond length, the larger the

13　electron cloud density value of the corresponding BCP.

14　　To investigate the microscopic features of the structure variation of the chelating

15　configuration B with H_2O, the interaction energy and average number of hydrogen

16　bonds of water molecules was calculated via molecular dynamics (MD) simulations.

17　The following can be used to calculate the interaction energy between the chelating

18　configuration B and the H_2O, which includes the van der Waals interaction energy (E_l),

19　electrostatic energy (E_e)[18], and the potential energy (E_{ie}):

$$E_{ie} = E_l + E_e$$

$$= \frac{1}{2}\sum_{i}^{N}\sum_{j\neq i}^{N}\frac{1}{4\pi\varepsilon}\frac{q_i q_j}{\varepsilon_r r_{ij}} + \frac{1}{2}\sum_{i}^{N}\sum_{j\neq i}^{N}4\varepsilon_{ij}\left[\left(\frac{\sigma_{ij}}{r_{ij}}\right)^{12} - \left(\frac{\sigma_{ij}}{r_{ij}}\right)^{6}\right]$$

20　　　　　　　　　　　　　　　　　　　　　　　　　　　　　　　　　　(1)

21　where ε is the dielectric constant, ε_r is the relative dielectric constant, q_i is the charge of

22　the ith atom, q_j is the charge of the jth atom, r_{ij} is the distance between two atoms, and

23　ε_{ij} and σ_{ij} are the Lennard-Jones parameters between the two atoms. The geometric

24　criteria of $\theta_{H\text{-}O\text{-}O} \leq 30°$ and $bond_{O\text{-}O} \leq 3.5$ Å were used to calculate the hydrogen bonds[19].

25　　As shown in Fig. 2g, the initial configuration for one simulation of chelating

26　configuration B filled with water molecules was produced with VMD[20]. The van der

27　Waals interaction energy and electrostatic energy were 0.0205 and -0.0011 kcal/mol,

respectively, and the interaction energy between chelating configuration B and the hydration layer was 0.0194 kcal/mol. The results indicate that the chelating configuration B and the hydration layer are mutually exclusive, which confirms that the chelating configuration B coordination mode is stable.

The average number of hydrogen bonds is 4.528, which supports that hydrogen bonds form between the water molecules and chelating configuration B. It also indicates that the hydrogen bonds capture the water molecules and form a dense hydrated layer. This results in both physical obstruction and energy barriers, which can enhance the coordination binding radiostability. Supplementary Fig. 11c shows the radial distribution function (RDF) between Lu and oxygen atom of the water molecule. The first peak occurs when the distance between the oxygen atom of the water molecule and Lu reaches 4.6 Å, which is more than the van der Waals radius between them (3.4 Å). It emerges that the phosphorylcholine hinders the formation of a hydrated layer, which indicates that chelating configuration B is stable.

The spatial density distribution function of water molecules can be visualized and shows that the density of water molecules within the neighborhood of Lu is obviously less than in other regions. This indicates that the hydration layer around chelating configuration B forms an energy barrier interaction that synergistically enhances the stability of this configuration (Fig. 2h). These results validate the coordination mechanism of PCMs with ^{177}Lu in a O,O-bidentate chelating configuration, which synergistically enhances the radioactive stability of PCMs bound to radionuclides based on a hydration layer mediated by hydrogen bonding.
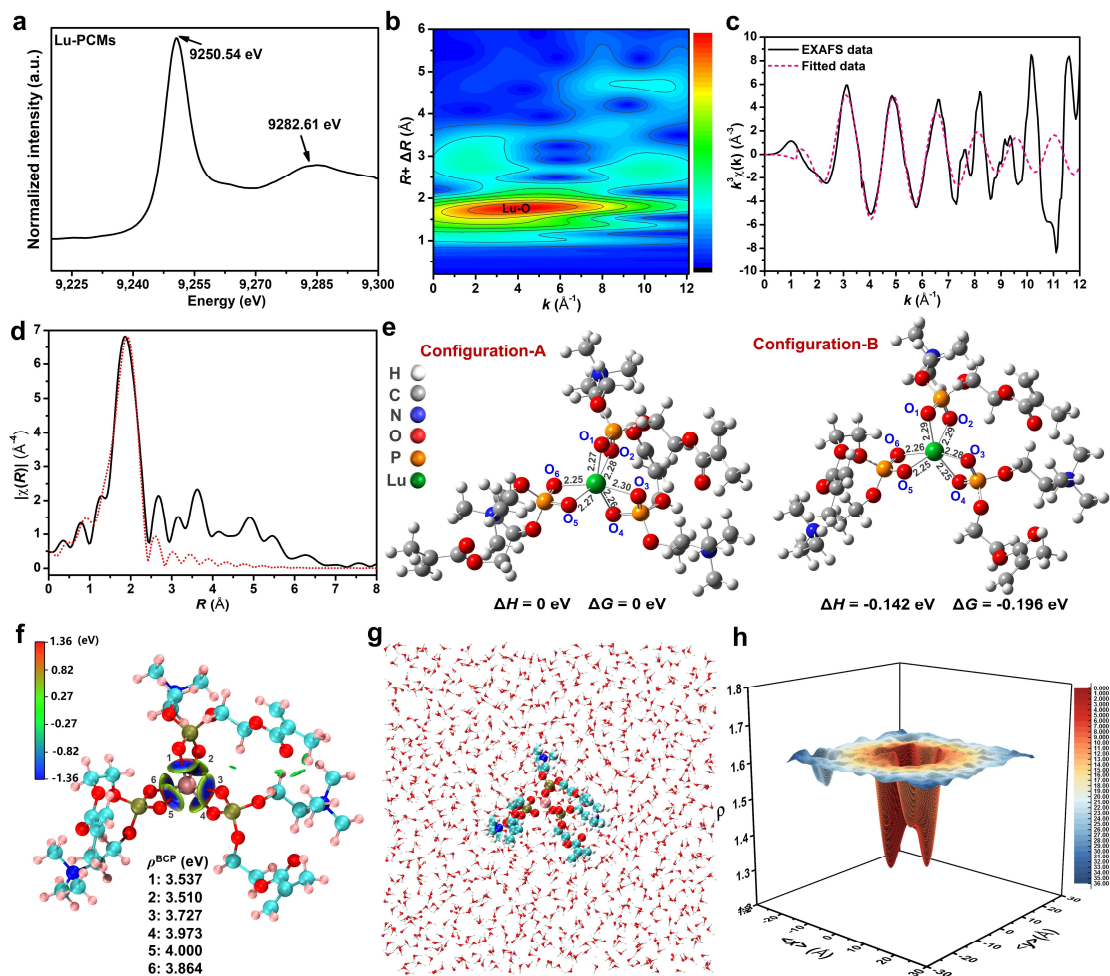
Fig. 2 Lu binding mechanism in the PCMs. a Normalized L_{III}-edge EXAFS profiles of the Lu-PCMs. **b** Wavelet transform for the k^3-weighted EXAFS signal of Lu-PCMs. **c** Lu L_{III}-edge k^3-weighted EXAFS spectra (black line) and the best theoretical fits (red dotted line) of the Lu-PCMs. **d** Corresponding nonphase shift corrected Fourier transforms. EXAFS data (black line) and fitted data (red dotted line) of the Lu-PCMs in R-space. **e** Structures of Lu complexes with phosphorylcholine obtained after geometry optimization at the B3LYP/SDD/6-31G(d,p) level of theory (6-31G(d,p) basis set was used for H, C, N, O, and P atoms; SDD for Lu were employed for geometry optimizations and frequency analysis), which is in agreement with the experimental EXAFS. The ΔH and ΔG were obtained via DFT calculation. A six-coordinate 3: 1 Lu complex with mixed coordination of the three ligands for Configuration-A and Configuration-B, and their relative binding enthalpies and Gibbs free energies indicated the Configuration-B coordination is more stable than that with Configuration-A

coordination. The bond distances in angstrom (Å) have been listed together with the structures. **f** IGMH maps of Lu-PCMs (Configuration-B). The three phosphorylcholines are respectively defined as the three fragments. Visual molecular dynamics (VMD) program renders IGMH quantitative analysis data to obtain a visualization of the intensity of ligand-Lu interactions. The bluer the color, the larger the contribution of the intermolecular interaction to Lu. The bond critical points and bond paths corresponding to Lu-O interactions are also shown in the IGMH image. Electron density values at the BCP are displayed by black texts. **g** Schematic of the MD simulation system for chelating configuration-B immersed in an open water environment. **h** The spatial density distribution function for water molecules, ρ, as a function of average coordinate component $<x>$ and $<y>$. The distances between Lu and oxygen atom of water molecules that projection on xy plane is used as color bar.

***In vitro* biocompatibility of PCMs.** A live/dead assay and cell counting kit-8 (CCK-8) assay were used to evaluate the influences of the PCMs on the viability and proliferation of cells. The CCK-8 results verified that PCMs do not inhibit cell proliferation, even when the concentration is increased up to 200 μg/mL of PCMs with 48 h of incubation (Supplementary Fig. 13a, c, and e). The live/dead staining results for 1 and 3 days showed that the PCMs have no obvious cytotoxicity on the cocultured human hepatocellular carcinoma cells (HepG2), human umbilical vein endothelial cells (HUVEC), and human normal liver cells (LO2), and the cells were not dead even when the concentration was increased up to 100 μg/mL of PCMs with 3 days of incubation (Supplementary Fig. 13b, d, and f).

To verify the hemocompatibility of PCMs, in vitro, blood coagulation and hemolysis tests were conducted using pig and human blood. Representative images are shown in Supplementary Fig. 14a and c. PCMs showed the same clotting time and clot volume, which increased over time in PBS and saline groups. As shown in Supplementary Fig. 14b and d, the hemolysis test showed that the PCMs had low hemolysis values, which were similar in the saline and PBS (both below 3%). The coagulation and hemolysis tests showed that PCMs do not have coagulation-promoting or hemolytic properties and

can exhibit hemocompatibility in blood comparable to that in saline and PBS. Thus, the PCMs have great prospects as a radioactive microsphere precursor due to their biocompatibility and nontoxicity.

Evaluation of local vascular distribution, embolism, radiostability of ^{177}Lu-PCMs, and safety of polymer embolized microspheres *in vivo*. Studies have shown that radioembolic microspheres with size in the range of 20-60 μm can be effectively deposited in the capillary bed of liver tumors to deliver localized high-radiation doses while sparing the surrounding healthy tissues[21]. Fluorescein isothiocyanate (FITC)-labeled PCMs with a median diameter of 42.2 μm (range, 30–60 μm) were injected into the transparent hepatic vascular bed of Wistar rat. The results showed that the microspheres can effectively deposit and embolize the corresponding vascular bed, especially the distal peripheral vessels of the liver (Fig. 3a). However, after injection of FITC-labeled PCMs, stereoscope images of intact rat decellularized livers showed that PCMs with particle size of 117.2 μm can only be dispersed and embolized in the trunk of intrahepatic vessels (Fig. 3b). An SEM image of the decellularized rat livers after injection of FITC-labeled PCMs showed that the microspheres still maintained regular spherical morphology in the blood vessels after injection, freezing, and drying, indicating that they had strong stability and compression resistance (Fig. 3c).

In the rabbit renal embolism model, the results showed an abundant vascular bed in the target kidney, which could be blocked immediately after embolization of PCMs under the guidance of digital subtraction angiography (DSA). An excellent vascular occlusion effect was maintained in comparison with the normal left kidney at 10, 20, and 30 minutes and even 21 days after embolization (Supplementary Fig. 15a, b). As shown in Fig. 3d, postoperative observation was performed on samples in vitro along with hematoxylin and eosin (H&E) staining of the target kidney. At 7 days after the embolization, the renal parenchyma of the embolized kidney showed hyperemia and edema compared with the contralateral normal kidney. Furthermore, HE staining showed partial necrosis. On the 14th day after embolization, the renal parenchyma blackened, and HE staining showed a large number of necrotic renal tissue cells. At 21

days after embolization, the renal parenchyma atrophied, and HE staining showed a large amount of severe tissue necrosis. More importantly, during the whole process of renal embolization in rabbits, the PCMs maintained a regular spherical shape in the tissue, which was not affected by the injection mode, tissue environment, and deposition time.

In the rabbit ear VX2 subcutaneous tumor models, the PCMs were injected into the rabbit ear blood-supply artery. The artery was then significantly embolized and blocked (Supplementary Fig. 16a, b). Laser speckle (LS) images at one day after the operation indicated that local blood supply of the subcutaneous tumor was significantly less than that of the blank group (Supplementary Fig. 16c, d). At three days after injection, the growth rate of the subcutaneous tumor was significantly inhibited (Supplementary Fig. 16a, e), suggesting that the PCMs can effectively deposit in the tumor blood supply artery, block it, and inhibit tumor growth. These results indicate that PCMs have excellent embolic and anti-tumor properties along with excellent mechanical stability *in vivo*.

The radiostability and biocompatibility of ^{177}Lu-PCMs were also evaluated by using a pig model of orthotopic liver embolization (Fig. 3e). Embolization was performed through puncture of the right femoral artery with a microcatheter under the guidance of DSA, showing an abundant hepatic artery vascular bed in the target liver segment before embolization. But after embolization with ^{177}Lu-PCMs, the vascular bed in the target liver segment was quickly and completely blocked, suggesting that the ^{177}Lu-PCMs still maintain good embolism in large animals (Fig. 3f). The experimental pig was euthanized 10 days after the surgery, and the liver and other major intact organs were taken for SPECT-CT scanning. The γ photon signal of ^{177}Lu-PCMs remained visualizable for 10 days after IAB, indicating good imaging performance. Encouragingly, the ^{177}Lu-PCMs were still stably fixed in the treated liver segment after 10 days of IAB, and no radioactivity was found in other major organs. This indicated that no pulmonary shunt occurred in PCMs, even in the absence of tumor microvascular beds, which prevented the development of radiation pneumonia (Fig. 3g).

To accurately trace the biodistribution and biometabolic distribution of ^{177}Lu, the

radioactivity of pig organs, tissues, urinary, and fecal matter was measured by γ-counter. As shown in Supplementary Fig. 17a, the radiation uptake rate was very low in other organs and tissues, but not in the target liver segment (62.74 ± 1.26 %ID/g), where the radiation uptake rate was high. The biometabolic distribution results showed the radiation uptake rate was also very low for urinary and fecal matter (Supplementary Fig. 17b). More importantly, TUNEL immunohistochemical staining showed a high apoptosis rate in the ^{177}Lu-PCMs-treated liver segment tissue (Fig. 3h), and it could be observed that blotting of ^{177}Lu-PCMs were neatly and regularly arranged in the hepatic artery vasculature. The carried ^{177}Lu is not eluted by local blood flow, resulting in no radionuclide diffusion and no radiation damage to non-target organs and tissues (Supplementary Fig. 17c). This shows the high radiostability *in vivo* and strong radionuclide loading ability of ^{177}Lu-PCMs.

The biochemical examination and blood cell count were also performed. The blood cell count of the experimental pigs was not abnormal before and after embolization, and the common reactions to interventional embolization brachytherapy returned to normal by 10 days post-operatively (Supplementary Fig. 17d, e). These results implied that the ^{177}Lu-PCMs had excellent biocompatibility *in vivo*, which is attributed to the phosphorylcholine ligands of PCMs acting synergistically with the hydration layer to prevent significant ^{177}Lu detachment, indicating great potential for clinical transformation.
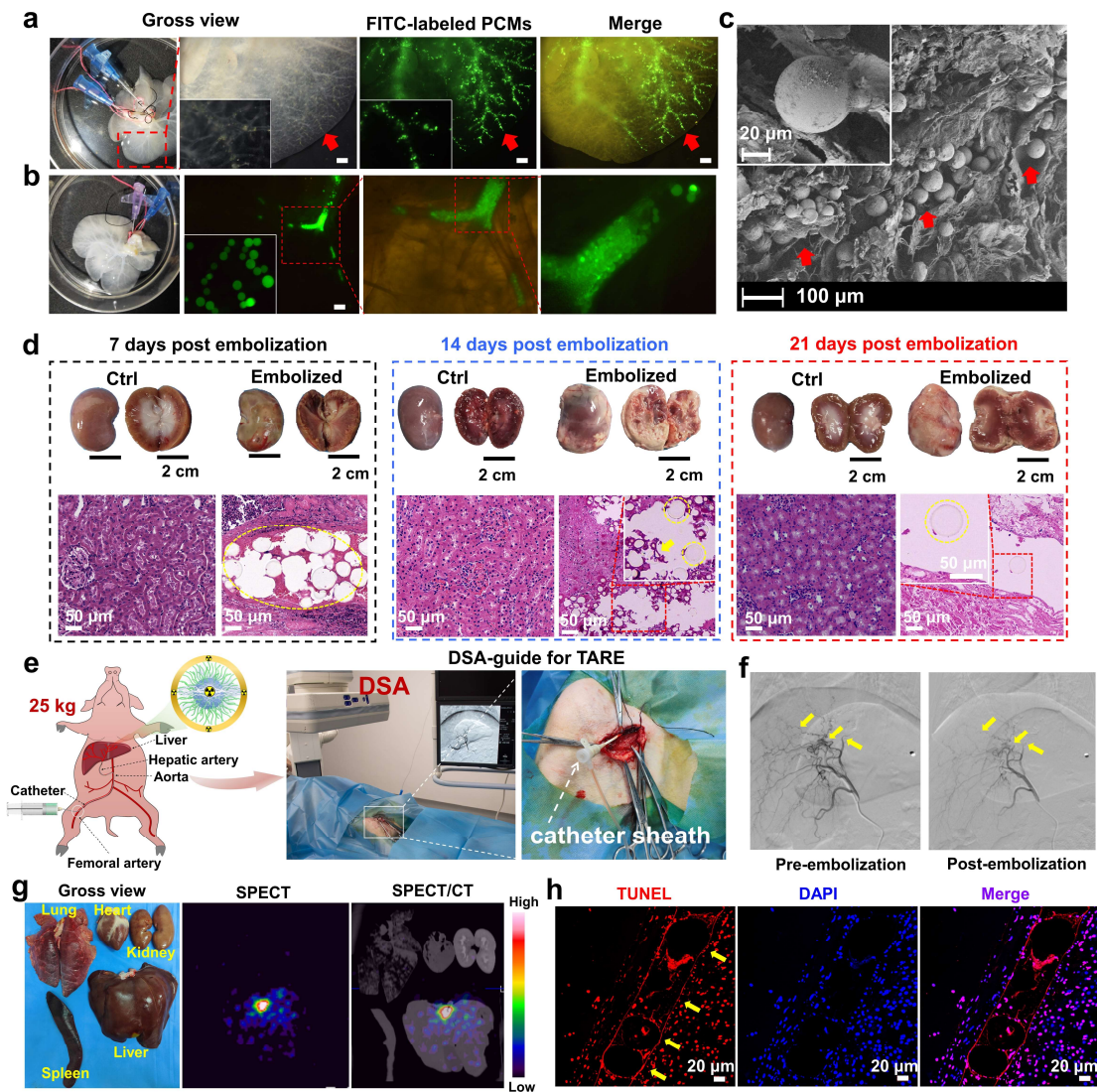
Fig. 3 Assessment of intravascular distribution of PCMs in the decellularized liver model, renal artery embolization in rabbits, and liver arterial embolization in a pig model using PCMs. a The stereoscope images of intact rat decellularized liver models after injection of FITC-labeled PCMs, it was verified that PCMs with a particle size of 42.2 μm can embolize into the distal end vessels of rat liver. Scale bar: 200 μm. **b** The stereoscope images of intact rat decellularized liver models after injection of FITC-labeled PCMs, it was verified that PCMs with a particle size of 117.2 μm can embolize into the proximal vessels of rat liver. **c** SEM image of rat decellularized liver models after injection of FITC-labeled PCMs. The inset shows a high-magnification image. **d** Gross view of excised kidneys, and corresponding representative H&E images of rabbit kidneys at 7, 14, and 21 days following embolization showing PCMs (yellow dashed circle) in the renal artery on stained histologic images. **e** Schematic demonstrating IAB in the pig model DSA-guided embolization of ^{177}Lu-PCMs (29.60

MBq) and a representative gross image of the evaluation process. **f** DSA images of internal liver artery before (arrow pointing the patent) (left), and after embolization (arrow pointing embolized with no blood flow) (right). **g** Gross view and SPECT/CT images of excised Heart, liver, spleen, lung, and kidney. **h** TUNEL and DAPI staining of representative resected target liver segment tissue.

***In vivo* interventional embolization IAB.** Due to the excellent in vitro and *in vivo* biocompatibility of ^{177}Lu-PCMs, we constructed an orthotopic rat model of liver cancer to validate the anti-tumor efficacy and SPECT imaging performance of ^{177}Lu-PCMs (Fig. 4a). Representative SPECT/CT images of the free ^{177}LuCl$_3$ control group show a significant spread of ^{177}Lu from the rat tumor site to the whole body over time, especially in the osteoarthritic cavity (Fig. 4b). Conversely, representative SPECT/CT images of the ^{177}Lu-PCMs group shows no ^{177}Lu uptake in other organs or tissues of the rats over time, indicating that ^{177}Lu-PCMs are very stable *in vivo*. This is attributed to the coordination mode of PCMs with ^{177}Lu, which hinders the off-targeting and diffusion of ^{177}Lu (Fig. 4c). Magnetic resonance imaging (MRI) results showed that treatment with PCMs only partially inhibited tumor growth compared to the saline control and free ^{177}LuCl$_3$ groups. This is attributed to the embolization of PCMs, thereby slowing down the tumor growth. ^{177}Lu-PCMs for IAB of the tumor yielded remarkable treatment effect. The complete tumor regression was achieved after 10 days of IAB (Fig. 4d, e), and there was no damage to the major organs (Supplementary Fig. 18).
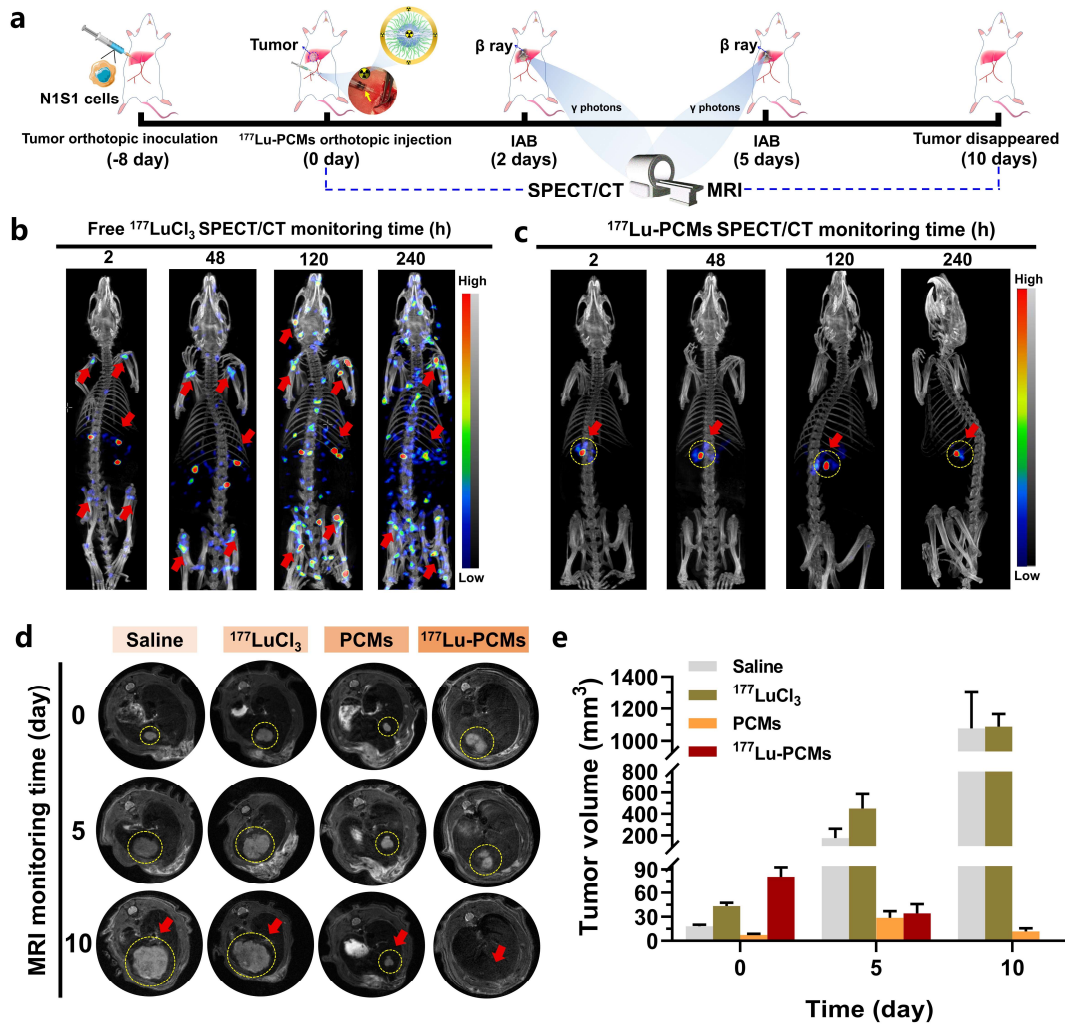
Fig. 4 *In vivo* IAB with ^{177}Lu-PCMs for rat N1S1 orthotopic live tumor model. **a** Schematic illustration shows the *in vivo* IAB procedure of rat liver tumor. **b** Representative SPECT/CT images of rat liver tumor at the different monitoring times after precision delivery of free ^{177}LuCl$_3$ (14.8 MBq) for tumor intravascular brachytherapy. The red arrows indicate the location of the uptake for ^{177}Lu. **c** Representative SPECT/CT images of orthotopic liver tumor-bearing rat at the different monitoring times after precision delivery of ^{177}Lu-PCMs (14.8 MBq) for intravascular brachytherapy. The red arrow shows the location of the tumors. **d** Representative MRI imaging of tumors after precision delivery of the saline, free ^{177}LuCl$_3$, PCMs, and ^{177}Lu-PCMs for 0, 5, and 10 days. The yellow dashed circles show the location of the IAB tumors. **e** Tumor volume of rat N1S1 orthotopic liver tumor model after IAB of saline, free ^{177}LuCl$_3$, PCMs, and ^{177}Lu-PCMs, respectively.

We employed ^{177}Lu-PCMs as a therapeutic agent for *in vivo* interventional IAB of rabbit VX2 liver tumor (Fig. 5a). The ^{177}Lu-PCMs were injected into the tumor under

the guidance of DSA for IAB. As shown in Supplementary Fig. 19, the microcatheter entered the hepatic artery, followed by injection of iohexol contrast agent. The location, size, and vascular supply of the tumor were visualized by DSA imaging. After precise injection of free $^{177}LuCl_3$ solution, the vessels could still be clearly observed with the iohexol contrast agent. After injection of PCMs or ^{177}Lu-PCMs, the tiny blood supply vessels of the tumor disappeared, which was attributed to the good embolic properties of the microspheres. SPECT/CT images of free $^{177}LuCl_3$ group showed a diffuse γ-photon signal throughout the body, suggesting that ^{177}Lu had spread throughout the body and was highly enriched in the spine and joint lumen (Fig. 5b). The ^{177}Lu-PCMs were deposited in the tumor area with an obviously high γ-photon signal, while the normal liver tissue and other areas of the body showed no obvious signal (Fig. 5c).

In vivo imaging system (IVIS) images of resected rabbit VX2 liver tumor and major organs were obtained 5 days after Cy 5.5-labeled PCM embolization (Supplementary Fig. 20a, b). Similarly, these images also revealed the stable distribution of microspheres within the tumor tissue with no pulmonary shunts or ectopic embolization of the normal heart, liver, spleen, and kidney (Supplementary Fig. 20c, d). On the 10th day postoperatively, all tissues collected from the ^{177}Lu-PCM group were tested by a γ-counter. The tumor tissue showed the highest radiation uptake of more than 16.5 %ID/g, while the other sites showed less than 2 %ID/g (Supplementary Fig. 21a). However, the radiation uptake in the tumor tissue in the free $^{177}LuCl_3$ group was only 1.61 % ID/g, which was mainly attributed to incomplete metabolism due to complexation of the protein with ^{177}Lu[22]. Higher ^{177}Lu uptake was observed in all other tissues and organs, especially the bones, liver, spleen, lungs, and kidneys. Therefore, ^{177}Lu-PCMS for TARE can avoid radiation damage to normal tissues *in vivo* and could improve the effectiveness and safety of *in vivo* applications.

The antitumor efficacy of ^{177}Lu-PCMs was further validated. As shown in Fig. 5d, after injection of free $^{177}LuCl_3$, T2WI images showed that the tumor continued to grow, diffusion-weighted imaging (DWI) and apparent diffusion coefficient (ADC) images also showed that the enhancement of tumor activity was not suppressed. Similarly, gadolinium ion complex-enhanced T1-weighted images (T1WI-Gd) images showed that the tumor blood supply was not well blocked. As expected, both the blank PCM group and the ^{177}Lu-PCM group showed inhibited tumors to some extent. The tumors in the blank PCM group were mildly suppressed thanks to the PCMs reducing the blood supply to the tumor tissues, resulting in slowing of the tumor growth. However, there

were more residual tumor tissues at the edges of the tumors in the blank PCM group compared with the ^{177}Lu-PCM group (Fig. 5e). Encouragingly, the tumor volume curves obtained by T2WI calculations showed that the tumor suppression ability of the ^{177}Lu-PCM group was more significant than that of the PCM group, and there was almost no tumor growth (Fig. 5f and Supplementary Fig. 21b). The quantitative analysis of ADC values from MRI revealed that the signal of the ^{177}Lu-PCM group was significantly enhanced after treatment compared with the blank PCM group, indicating more significant liquefaction and necrosis of tumor tissue (Supplementary Fig. 21c). These results confirm that TARE with ^{177}Lu-PCMs has a good tumor-suppressive effect on HCC under the guidance of DSA, SPECT/CT, and MRI imaging. Furthermore, ^{177}Lu does not desorb from the microspheres, which would not result in side effects associated with systemic radiation damage.

After 10 days of treatment of experimental rabbits, tumor sections were collected for immunostaining. The H&E-stained tumor sections showed that the ^{177}Lu-PCMs treatment group had the most pronounced tumor-cell injury and apoptosis compared to the ^{177}LuCl$_3$ group and PCM group. Ki-67 immunohistochemical staining and TUNEL staining showed the highest tumor cell accretion rate in the ^{177}LuCl3 group and the highest apoptosis rate in the ^{177}Lu-PCM-treated group. The fluorescence section map of vascular endothelial growth factor (VEGF) staining showed that the ^{177}Lu-PCM group had the lowest tumor tissue staining rate. This indicates that ^{177}Lu-PCMs may inhibit the expression of neovascularization factor and prevent the formation of neovascularization for tumor metastasis. ^{177}Lu emits β-particles ($E_{\beta(max)} = 0.497$ MeV) that trigger DNA double-strand breaks[23]. The γ-H$_2$AX-stained section maps showed that ^{177}Lu-PCMs kill tumor cells mainly by damaging their DNA through radioactive β particles (Supplementary Fig. 21d). All the results demonstrate that ^{177}Lu-PCMs can selectively irradiate tumors internally by IAB. This leads to tumor cell apoptosis and possibly prevents tumor metastasis and recurrence after treatment.

The radioactive microsphere brachytherapy can promote systemic immune activation[24] (Supplementary Fig. 22a). By analyzing T cells in tumor tissues, we found that the tumors of animals treated with ^{177}Lu-PCMS had significant T cell infiltration (Supplementary Fig. 22b). Flow cytometry results showed that the proportion of CD8$^+$ T cell subsets in tumors increased significantly after ^{177}Lu-PCMS treatment, and the differentiation of CD8$^+$ T cells was promoted with the increase in the radiation dose (Supplementary Fig. 22c-f). These results suggest that ^{177}Lu-PCMS therapy can induce

an immune response, promote the enrichment of T cells in the tumor microenvironment, and promote the differentiation of CD8^{+} T cells.

Next, we investigated the biosafety of the treatments. H&E staining of major organs verified that ^{177}Lu-PCMs did not cause significant inflammation or injury (Supplementary Fig. 23a). We tested biochemical indicators such as glutamic aminotransferase (AST), alkaline phosphatase (ALP), albumin (ALB), alkaline phosphatase (ALP), and creatinine (CREA). No significant abnormalities occurred in the relevant indicators in the experimental rabbits compared with normal rabbits, and the fluctuations of the indicators fell within the normal range of TARE surgery (Supplementary Fig. 23b). We also tested blood-routine indexes such as white blood cells (WBC), red blood cells (RBC), hemoglobin (HGB), and platelets (PLT) in whole blood, and no significant abnormalities were found (Supplementary Fig. 23c). These results indicated that ^{177}Lu-PCMs did not cause significant harmful conditions to liver function and blood cells, confirming the biosafety of IAB.

***Ex vivo* anti-tumor efficacy of ^{177}Lu-PCMs in human resected liver tumors.** To demonstrate whether ^{177}Lu-PCMs can directly kill human liver cancer tumor tissues and cells, we collected 10 freshly resected human liver tumors and directly injected ^{177}Lu-PCMs into the tumor tissues (Fig. 5g). Tumor tissues were photographed (Fig. 5h), and SPECT/CT images were obtained 0 and 3 days after injection, showing ^{177}Lu existed at the injection site of the human resected liver tumor (Fig. 5i). Histologic evaluation of the injected area showed good anti-tumor effects with little nuclear staining of tumor cells that was in stark comparison to the untreated tumor tissues (Fig. 5j and Supplementary Fig. 24), and ^{177}Lu-PCMs in the tumor injection area could be observed without degradation. These findings are consistent with those obtained from rat and rabbit tumor models.
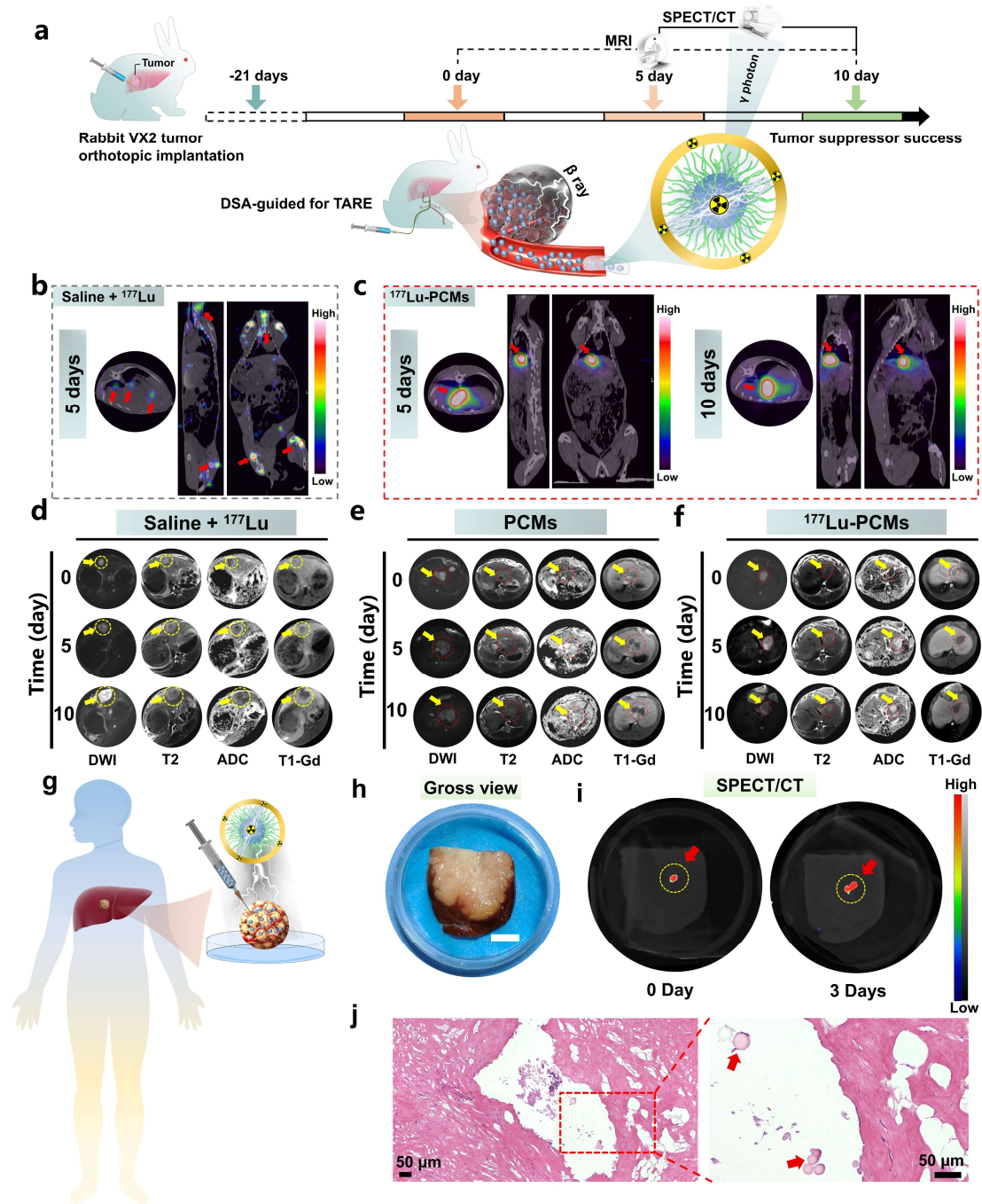
Fig. 5 DSA-guided precision delivery of ^{177}Lu-PCMs into the rabbit VX2 liver tumor model and therapeutic effect evaluation. **a** Schematic diagram of the modeling, treatment, and monitoring regime used rabbit VX2 liver tumor model. **b** SPECT/CT images of rabbit VX2 liver tumor at 5 days after DSA-guided precision delivery of ^{177}LuCl$_3$ for tumor intravascular brachytherapy (The red arrows indicate the location of the uptake for ^{177}Lu). **c** SPECT/CT images of orthotopic liver cancer-bearing rabbit at 5 and 10 days after DSA-guided precision delivery of ^{177}Lu-PCMs for tumor intravascular brachytherapy (The red arrows indicate the location of the tumor).

Representative MRI imaging of tumors after embolization with the ^{177}LuCl$_3$ (**d**), PCMs (**e**), and ^{177}Lu-PCMs (**f**) for 0, 5, and 10 days. The yellow arrow shows the location of the intravascular brachytherapy tumors. **g** Schematic illustration of ^{177}Lu-PCMs injected into human resected liver tumor. **h** Gross view of representative human resected liver tumor. Scale bar: 1 cm. **i** Representative SPECT/CT imaging of human resected liver tumor at 0 and 3 days after ^{177}Lu-PCMs injection. **j** H&E staining of the representative human resected liver tumor after treated with ^{177}Lu-PCMs. The red arrows indicate the location of the ^{177}Lu-PCMs.

3 Discussion

Our results provide evidence that SPECT-guided locoregional intravascular injection of ^{177}Lu-PCMs can be a safe and feasible means of hepatocellular carcinoma treatment. By integrating emulsion suspension polymerization and radiation-induced graft polymerization, we demonstrate a powerful universal radioactive microsphere strategy that can achieve large-scale fabrication, ultra-stable radiolabeling, and effective tumor control while meeting efficacy criteria for anti-tumor treatment. ^{177}Lu-PCM brachytherapy, embolic radio-theranostic properties were maintained without any degradation, ectopic embolization and adverse reactions, thus meet the safety criteria for clinical application.

We have compared commercially available radioactive microspheres with ^{177}Lu-PCMs (Table S3). ^{177}Lu-PCMs could be cheap local manufacture, with no leaching, and carrier-free suspension, minimizing hematogenous and systemic exposure. The density of the ^{177}Lu-PCMs was closest to that of blood and was more readily distributed uniformly in the vascular bed compared to the three commercially available microspheres, resulting in better prediction of pulmonary shunt and intrahepatic biodistribution. However, lung absorbed doses are significantly overestimated by ^{99m}Tc-MAA pretreatment SPECT imaging-guide diagnostic in clinical practice[25]. A downside of ^{166}Ho-scout is that it is not as readily available as ^{99m}Tc-MAA, which can be easily extracted from a generator. ^{166}Ho-scout needs to be ordered, activated in a nuclear reactor, and delivered to the treatment site[26]. ^{177}Lu-PCMs-scout could offer significant advantages during reconnaissance, and this reduces the chance that a patient is unnecessarily excluded from therapy or receives an unnecessary dose reduction. Above all, the SPECT imaging-guide diagnosis offers a noninvasive way to track the ^{177}Lu-PCMs in *vivo*.

We believe it is important to report results from this pilot study in precision medicine for several reasons. The two-step ESP-RIGP procedure has not been described previously to our knowledge. Theoretical DFT calculations confirmed that the ^{177}Lu loading mechanisms involve the formation of a stable complex *via* three phosphorylcholines in a cooperative ligand complexation with hydration layer synergy. This resulted in high radiostability *in vitro* and *in vivo* and strong radionuclide loading ability of ^{177}Lu-PCMs, which is consistent with our experimental findings. The first-principles DFT calculations for the RIGP reaction could also be reconfigured to continuously guide the design of next-generation radioactive microsphere precursors. Notably, the mild and simple preparation process by ESP-RIGP technology of the material is suitable for scale-up production with low preparation cost. The obtained ^{177}Lu-PCMs are mechanically more robust than commercially available radioactive microspheres and feature better theranostic properties *in vivo*. Besides good brachytherapeutic efficacy against tumors, ^{177}Lu-PCMs exhibit potential application as an anti-angiogenic inhibitor and immune checkpoint inhibitor carrier as personalized and multifunctional engineered radioactive microspheres for delivering anti-angiogenic drugs, immune checkpoint inhibitors, or other therapeutic agents with the long-term stability of drugs in the lesion area. In a clinical setting, IB with ^{177}Lu-PCMs has the potential to significantly improve survival outcomes in HCC. This could allow more patients to receive other procedures, such as liver transplantation and surgical resection. Particularly, radioactive lobectomy and radioactive segmental resection are expected to move the clinical application of ^{177}Lu-PCMs from palliative care to translational and radical treatment.

Methods

Materials. Ethenylbenzene (EB), polyvinyl alcohol (PVA), azodiisobutyronitrile (AIBN), acrylic acid (AA), 2-methacryloyloxy ethyl phosphorylcholine (MPC), anhydrous ethanol (99%), lutetium trichloride hydrate (LuCl$_3$·6H$_2$O), and nitric acid (HNO3), were purchased from Sinopharm Chemical Reagent Company. All chemicals from commercial sources were analytical grade and used without further purification. Nitrogen gas (99.99% purity) was obtained from Shanghai Louyang Gas Canned Co., Ltd. The 1,000 ppm standard solutions of lutetium (Lu) were purchased from SPEX Certi Prep, Inc. High-purity deionized water (PALL, Cascada BIO) was used for all experiments unless otherwise stated. [177]LuCl$_3$ solution (pH: 1.5) was purchased from

Chengdu Xinke Pharmaceutical Co., Ltd. Pentobarbital sodium was purchased from Lulong Biotechnology Co., Ltd. (Shanghai, China). Interventional medical devices were available from the Radiology Department of Xiang'an Hospital of Xiamen University.

Preparation of PEBMs. The poly(EB) microspheres (PEBMs) were prepared via the emulsion suspension polymerization (ESP) technology. Briefly, A 2% aqueous solution of PVA was prepared as a stabilizer for the emulsion suspension polymerization reaction by weighing 12 g of PVA dissolved in 0.6 L of deionized water, which was added to a 1 kg glass reactor (purchased from Shanghai Cancun Instruments & Equipment Co., Ltd.) with a stirring speed of 120 rpm/min to form a homogeneous phase system. After bubbling with N_2 for 20 min, the system temperature was increased to 80 °C. Then a mixture of EB (8 wt%) and AIBN (0.5 wt%) was added dropwise (0.6 mL/min) via a syringe pump with constant stirring speed, and the reaction was terminated by natural cooling under a nitrogen atmosphere for 6 h. The white emulsion was centrifuged at 6000 rpm/min. The white emulsion was centrifuged and settled at 6000 rpm/min, the supernatant was removed, the bottom layer of microspheres was cleaned by ultrasonication by adding anhydrous ethanol, and then the operation was repeated 5 times by centrifugal settling and washing, and finally, the white powdered PEBMs were obtained by vacuum drying for 24 h.

Synthesis of PCMs. The phosphorylcholine-modified coordination polymeric microspheres (PCMs) were synthesized by the ^{60}Co γ-rays radiation-induced co-grafting polymerization (RIGP) technology. Briefly, 30 g of PEBMs were weighed and placed in a cobalt (^{60}Co) source (Shanghai Institute of Applied Physics, Chinese Academy of Sciences provides cobalt source irradiation services) under nitrogen gas for pre-irradiation. The absorbed dose was 200 kGy, followed by the addition of 0.6 L of deionized water, 2 wt% AA, and 10 wt% MPC to a 1 kg glass reactor, stirred at 100 rpm/min for 30 min at room temperature, and then removed by bubbling with nitrogen for 20 min. After the oxygen was removed by bubbling with nitrogen for 20 min, 30 g of pre-irradiated PEBMs were added to the system, and the system was sealed after 20 min of continued N_2. At the end of the reaction, the reaction product was centrifuged at 6000 rpm/min to remove the supernatant, and the bottom layer of modified microspheres was washed by ultrasonication with deionized water to remove the polyacrylic acid homopolymer. Then, the operation was repeated 5 times by centrifugal

sedimentation and washing, and finally, the white powdered PCMs were obtained by vacuum drying for 24 h.

Preparation of ^{177}Lu-PCMs. ^{177}LuCl$_3$ solution (pH: 1.5, 37-296 MBq) was added to saline containing PCMs (10 mg/mL) and sonicated for 20 min at 45 °C (Accelerate the coordination chelation of PCMs with ^{177}Lu), and adjusted pH to 12-13 with potassium phosphate solution. Then, the obtained mixture was centrifuged at 4000 rpm/min for 5 min to remove the supernatant, and then washed and centrifuged three times using physiological saline to remove the free ^{177}LuCl$_3$, and finally, ^{177}Lu-PCMs were obtained.

Physiochemical characterization. Fourier-transform infrared (FT-IR) spectra were collected on a Nicolet Avatar 370 FTIR spectrometer (Thermo Nicolet Company, USA) in attenuated total reflectance mode with a resolution of 4 cm^{-1} and 32 scans.

The elemental composition and chemical states of the fibers were analyzed by X-ray photoelectron spectroscopy (XPS) using a Thermo SCIENTIFIC ESCALAB 250Xi instrument. The XPS data were acquired through wide scans ranging from 0 to 1200 eV.

AFM images were taken on a Bruker Multimode V, using Tapping Mode and a scan speed of 2.0 Hz. The samples for AFM measurement were dripped directly onto the clean silicon wafer.

DLS measurements were performed with a Malvern Mastersizer 3000.

The test method of microsphere density is the gas displacement method, the specific steps include: 1, first test the volume of the empty tube; 2, using helium as the medium, gas displacement pressure equilibrium to measure the free volume after the sample with microspheres, the difference between the front and back volume is the volume of microspheres; 3, according to the ratio of microsphere mass and microsphere volume can obtain the true density of microspheres.

X-ray diffraction (XRD) analysis was performed on a RIGAKU D/Max2200 XRD instrument. Nitrogen adsorption-desorption isotherms were measured by a surface aperture adsorption instrument (ASAP2010C, Micromeritics, USA).

The specific surface areas of the samples were calculated using the Brunauer–Emmett–Teller (BET) method within a relative pressure (P/P$_0$) range of 0.0–1.0, and the pore size distribution was calculated by the Barret–Joyner–Halenda (BJH)

algorithm.

The surface morphology of the samples and the energy dispersive spectroscopy (EDS) analysis were performed using field-emission scanning electron microscopy (SEM) (JSM-6700F, JEOL, Japan). All the samples were sputtered with gold to enhance the electron conductivity before observation.

A contact angle experiment was used to analyze the hydrophilic and hydrophobic properties of samples by a KSV Instrument. The samples were fixed upon the specimen stage. A drop of 5 μL distilled water was dropped onto the surface of the sample. Photographs were recorded with a NAVITAR camera to analyze the contact angle. The angle of the contact point between water droplets and the sample surface was regarded as the contact angle of the sample. Each sample was measured five times at different locations on the surface.

Theoretical calculations Computational methods. All density functional theory (DFT) simulations were executed using the Gaussian 09 software package for reactant and product paths. Geometries were optimized using the B3LYP method[27] with a 6-31G(d,p) basis set[28]. SDD for Lu were employed for geometry optimizations and frequency analysis. Transition states with only one imaginary frequency were located using the Berny algorithm at the level of 6-31G(d,p)[28], and intrinsic reaction path (IRC) calculations were performed to verify whether the detected saddle point corresponded to the expected reactant and product paths.

NEXAFS Characterizations. The near-edge X-ray absorption fine structure (NEXAFS) of O K-edge was measured at the soft X-ray magnetic circular dichroism end station (XMCD) of the National Synchrotron Radiation Laboratory (NSRL) at the University of Science and Technology of China (USTC).

EXAFS Characterizations. The extended X-ray absorption fine structure (EXAFS) at the lutetium L_3-edge was measured in fluorescence mode using a solid-state Ge fluorescence detector on the XAS beamline at the Australian Synchrotron, ANSTO Melbourne. Standard procedures were followed to analyze the EXAFS data using the software package Demeter[29]. The backscattering amplitude and phase shift were

calculated with the program FEFF 9[30]. Fourier transform (FT) was performed on the k^3-weighted EXAFS oscillations from 2.3 to 10.5 Å^{-1}. A window of 1.0−2.7 Å in r-space was used for the curve fitting of FT-EXAFS data. Amplitude reduction factor S_0^2 value of 0.95 was used. Structural parameters, such as coordination numbers (CN), bond distance (R), Debye-Waller factor (σ^2), and inner potential shift (ΔE_0), were obtained from the fitting.

DFT calculation method. To save computational efficiency, a unit of PCMs was chosen as a computational model. Density-functional calculations were implemented in the Gaussian 09 program[31] using the B3LYP level of theory[32], which has been widely utilized and proven to be sufficiently accurate for extensive systems. 6-31G(d,p) basis set was used for H, C, N, O, and P atoms; SDD for Lu was employed for geometry optimizations and frequency analysis. It is worth noting that the reliability of the computational setup has been also justified and that the structural properties after optimization agree well with experiments. Frequency calculations were performed to verify that geometries were minima.

IGMH method. The IGMH quantitative analysis was implemented by Multiwfn 3.7[33], while the visualization of the interaction strength was obtained by the VMD 1.9.3 program[20].

MD simulation method. The molecular dynamics simulations were performed by using LAMMPS[34] with the TIP3P water model[35]. The long-range electrostatic interactions were computed by using the particle-particle, particle–mesh method[36]. The MD simulation system contains 3765 water molecules and chelating configuration-B (3 zwitterionic molecules and Lu) in periodic boundary conditions (box size 5.0 × 5.0 × 5.0 nm). The Lennard-Jones interaction parameters for oxygen atoms of water molecules are ε_{OO} = 0.1521 kCal/mol and σ_{OO}=3.15 Å[19]. The Lennard-Jones parameters for C, N, P atoms of chelating configuration-B and Lu are set according to the universal force field[37]. The time step is set to be 1 fs. The equilibrium simulations are performed in a NVT (canonical) ensemble with Nose-Hoover thermal bath at T=300 K for 50 ns.

Radiolabeling efficiency test. Radiolabeling efficiency was investigated using a Mini-

1   Scan Instant Thin Layer Chromatography Scanner (TLC; BioScan, USA)

2   **Imaging performance of the ^{177}Lu-PCMs in *vitro*.** To evaluate the imaging capacity

3   of ^{177}Lu-PCMs, a phantom study was first conducted. A series of ^{177}LuCl$_3$ and ^{177}Lu-

4   PCMs with different radioactivity (7.4, 14.8, 22.2, 29.6, and 37 MBq) achieved by

5   adjusting the amount of ^{177}Lu labeling were prepared. After centrifugal precipitation,

6   SPECT/CT imaging was performed with a nanoScan-SPECT/CT scanner (Mediso,

7   Hungary).

8   **In *vitro* radiostability test of the ^{177}Lu-PCMs.** The labeled radioactive microspheres

9   ^{177}Lu-PCMs were divided into two groups of three samples each with approximately

10   18.5 MBq each. The two groups of samples were added with 1.2 mL of physiological

11   saline and human serum (collected from the healthy blood of the first author, Xiao Xu),

12   and then the microsphere suspensions and supernatants were then taken at 1, 6, 24, 48,

13   72, 120, 192 and 240 h, respectively. Subsequently, analyzed by γ-counter (WIZARD

14   2480, Perkin-Elmer, USA) to measure the activity of the supernatant solution and the

15   microsphere suspension, and the radiostability curves of the ^{177}Lu-PCMs in saline and

16   human serum were obtained. The radioactivity was measured with a γ-counter

17   (WIZARD 2480, Perkin-Elmer, USA).

18   **Cell biocompatibility.** The human hepatocellular carcinoma cells (HepG2), Human

19   umbilical vein endothelial cells (HUVEC), and Human normal liver cells (LO2) was

20   obtained from American Type Culture Collection (ATCC, Manassas, VA, USA) and

21   was used throughout this study. To test the cytocompatibility of the PCMs, HepG2,

22   HUVEC, and LO2 cells were seeded into 96-well plates (5 x 103 cells per well).

23   Different concentrations of PCMs (0, 20, 40, 60, 80, 100, 150, and 200 μg/mL) were

24   added to the medium. 24 h and 48 later, 10 μL CCK-8 solution was added. After

25   incubating at 37 °C for 2 h, optical density at 450 nm (OD450) was measured for each

26   sample. Cell viability was calculated using the formula: $(OD_{test} - OD_{blank})/(OD_{control} -$

27   $OD_{blank})$. Cells were identified by Live/Dead staining assay after coculture for 1 and 3

28   days. For the Live/Dead staining assay, the cells were incubated with Calcein-

29   AM/propidium iodide (Solarbio, China) for 30 min and examined using a fluorescence

1   microscope.

2   **Clotting time measurement.** PBS (50 μL), normal saline (9 g/L, 50 μL), calcium

3   chloride (CaCl$_2$) solution (0.1 M, 50 μL) and PCMs dispersions of normal saline (10

4   mg/mL, 50 μL) were added to sequential wells on a 96-well plate. Subsequently, 50 μL

5   of human (collected from the healthy blood of the first author, Xiao Xu) or pig

6   (collected from the healthy Yorkshire pig) whole blood was added to each well. The

7   wells were rinsed with normal saline at selected time points to stop clotting, and the

8   fluid was repeatedly washed and withdrawn until the solution became clear, indicating

9   that all soluble blood components were removed. After completion of the test, clotting

10 time and clot formation in each well were recorded. All experiments using human blood

11 from healthy adult volunteers were carried out with informed consent and were

12 approved by the Medical Ethics Committee of the School of Public Health of Xiamen

13 University.

14 **Hemolytic test.** 3.0 mL of whole blood from a human or pig was added to a centrifuge

15 tube, washed with 1.0% sodium heparin, mixed with an equal volume of normal saline,

16 and centrifuged (1500 rpm, 10 min). The supernatant was removed, the precipitate was

17 mixed with 5-10 times the volume of normal saline, and the above procedure was

18 repeated three times to obtain red cell suspension (RCS). Mix 500 μL of RCS with 25

19 mL of normal saline to make a 2.0% RCS dilution. PBS (100 μL), normal saline (100

20 μL), ultrapure water (100 μL), and PCMs dispersions of normal saline (1 mg/mL, 100

21 μL) were added to sequential wells on a 96-well plate, and 100 μL of RCS (2.0%)

22 solution was added to each well. The above steps were repeated 6 times, and centrifuged

23 (1500 rpm, 10 min) after 1.5 h in a constant temperature chamber at 37 °C. 100 μL of

24 supernatant was taken from each well in a new well for the determination of optical

25 density (OD) at 540 nm using a Spectrophotometer. The hemolysis ratio was calculated

26 by the formula

27 hemolysis ratio (%) = $(OD_g-OD_n)/(OD_p-OD_n) * 100$

28 where OD_g, OD_p, and OD_n are the OD values of PCMs dispersion, positive control, and

29 negative control, respectively.

Preparation of decellularized liver model and assess the intravascular distribution of PCMs in the liver. After normal liver and liver N1S1 tumor-bearing of Wistar rats were completely excised, the portal and inferior vena cava of rat livers were washed with prepared 0.5%-1% sodium dodecyl sulfate (SDS) solution using a peristaltic pump (speed: 4 mL/min) for 12 h until the livers were translucent, and then rinsed with saline to remove residual SDS. drug release was determined as determined by the following method. Subsequently, 0.6 mL of fluorescein isothiocyanate (FITC)-labeled PCMs (10 mg/mL) of different particle sizes were slowly injected into the inferior vena cava of the liver using a 1 mL syringe, and images were immediately captured by fluorescence microscopy. The captured images were analyzed using Image J software.

Renal artery embolization on normal rabbits. The renal artery embolization of PCMs was performed on the right kidney of normal New Zealand rabbits. 3 rabbits after fasting for 12 h, and anesthetized by intravenous injection of 3% sodium pentobarbital (10-20 mg/kg). The rabbits were fixed in the supine position. Their groin skins were dissected, and the femoral arteries were separated using ophthalmic forceps. After the ligation of the distal arteries, a 2.1 F coaxial microcatheter (Terumo, Tokyo, Japan) was introduced into the proximal renal arteries using an 18-gauge puncture needle. The angiography of the rabbit renal arteries was firstly performed by injecting iohexol (Omnipaque, 300 mg iodine/mL, 0.5 mL/s) as a contrast agent. Then, 2.8 mL of PCMs (10 mg/mL, saline as dispersant) were slowly injected into the rabbit's right kidneys. After administration, iohexol was injected to detect rabbit renal embolism in DSA subtraction mode, and images were collected. After withdrawing the microcatheter and suturing the wound, the antibiotic ampicillin (50,000-200,000 units/kg, twice daily) was injected intramuscularly into experimental rabbits 3 days after the operation to prevent wound infection and inflammation. Subsequently, the rabbits were euthanized after rabbit renal embolism for 7 days, 14 days, and 21 days, and the samples of embolized right kidney and kidney normal left kidney were collected and fixed in 4.0% of paraformaldehyde in phosphate-buffered saline for preparation of tissue sections and hematoxylin and eosin (H&E) staining. Furthermore, before

euthanasia of rabbits 21 days after renal embolization, renal artery angiography was performed under DSA imaging guidance on the normal left and embolized right kidneys of rabbits to observe the embolization.

Construction of rabbit ear tumor-bearing model and treatment of tumors by endovascular embolization in *vivo*. 2.5-3 kg New Zealand White rabbits of either sex were purchased from Shanghai SLAC Laboratory Animal Co. VX2 tumor blocks were purchased from Shanghai Lalan Biotechnology Co. Initially, fresh tumor blocks were selected and trimmed to approximately 1 mm^3 in size. After the rabbits were put under light anesthesia, the prepared fresh tumor blocks of 1 mm^3 size were delivered subcutaneously into the rabbits' ears using an 18-gauge cannula. Then, rabbits carrying VX2 subcutaneous tumors of the ear were randomly divided into two groups (n=3). (1) saline; (2) PCMs (0.6 mL per rabbit). Saline or PCMs were injected into the subcutaneous tumors of rabbit ears by embolization under the guidance of DSA. Briefly, rabbits with subcutaneous tumors in VX2 ears were anesthetized by intravenous injection of 3% sodium pentobarbital (10-20 mg/kg) then, under the real-time guidance of DSA, a disposable medical sterile intravenous infusion needle was inserted into the subcutaneous tumor blood supply vessels, and then, subcutaneous tumor blood supply angiography was performed to locate the rabbit VX2 ear subcutaneous tumors. Subsequently, saline or PCMs were pushed into the subcutaneous tumor of the ear at a uniform and slow rate to avoid reflux. After administration, iohexol was injected in DSA subtraction mode to detect subcutaneous tumor vascular embolization in the ear, and images were collected. A laser scatter system was used to image the rabbit VX2 subcutaneous ear tumor to view blood flow during this period.

Hepatic artery radioembolization in Pigs. Three healthy Yorkshire pigs, weighing 25–30 kg, and specified pathogen-free, were obtained from the Shanghai JiaGan Biotechnology Co., Ltd., Shanghai, China. A 2-week acclimatization period was allowed. The animals were kept under conventional conditions with ad libitum access to tap water and given standard pelleted feed twice a day. The experiments were conducted in agreement with the Animal Care and Use Committee (CC/ACUCC) of

Xiamen University and approved by the ethical committee for animal experimentation of Xiamen University (XMULAC20210102). All healthy Yorkshire pigs were induced by intramuscular injection of sumitoxin-II (0.04 mL/kg) for pre anesthesia induction, establish a pathway through the ear marginal vein, maintain the anesthesia with propofol, and the anesthesia depth should be the disappearance of eyelash reflex. Transcutaneous oxyhemoglobin saturation, end-tidal CO_2 concentration, inspired oxygen fraction, and the core temperature was monitored and documented throughout the procedure. DSA-guide femoral artery access was performed to place a 5 F artery sheath followed by introducing a 2.1-F microcatheter and coaxial micro-guide wire. Then, liver arteriography was performed to locate the vascular bed in the target liver segment of pigs. Subsequently, ^{177}Lu-PCMs were manually pushed into the target liver segment of pigs through the microcatheter at a uniform and slow speed. After administration, iohexol was injected to detect target liver segment vascular embolism in DSA subtraction mode, and images were collected. Blood was collected from the experimental pigs on postoperative 0, 5, and 10 days for routine blood and biochemical analysis to assess the postoperative bone marrow suppression and liver and kidney function. Euthanasia was performed postoperatively after 10 days according to the experimental design, and the target embolized liver segments and important organ tissues (Hearts, liver, spleen, lung, and kidney) were taken for SPECT/CT (Siemens Symbia T16, Germany) imaging-guided scanning after intravascular brachytherapy of 10 days to the measured distribution of ^{177}Lu in important organ tissues to assess the radiostability of ^{177}Lu-PCMs. Then, histological examination to analyze and assess the biocompatibility of ^{177}Lu-PCMs. The samples of the ^{177}Lu-PCM-treated liver segment tissue were collected and fixed in 4.0% of paraformaldehyde in phosphate-buffered saline for preparation of tissue sections and immunofluorescence staining with terminal deoxynucleotidyl transferase dUTP nick end labeling (TUNEL), imaging was conducted with the electron microscope and fluorescence electron microscope, respectively.

Construction of rat liver tumor and rabbit VX2 liver tumor model. Animal care

and experimental procedures were approved by the Animal Care and Use Committee

(CC/ACUCC) of Xiamen University. Wistar rats (100-120 g, specific pathogen-free)

were used as experimental animals in this study. N1S1 cells were incubated in

suspension culture flasks and incubated at 37 °C under 5% CO_2 until reaching the

inoculation amount. To establish the rat liver tumor model, 0.2 mL of N1S1 cell

suspension (20×10^6 cells per 100 μL of PBS) was injected into the left lateral lobe of

the liver for each Wistar rat after a mini-laparotomy. Wistar rats were kept in a clean

environment at the laboratory animal center and tumors were allowed to grow for 8

days. After 8 days, the MRI images at 9.4 T were recorded on a Bruker Biospin 9.4 T

animal MRI scanner (Bruker, Germany) and were performed to diagnostic monitoring

the growth and the size of the liver tumors. The 2.5-3kg of New Zealand white rabbits

were purchased from Shanghai SLAC Laboratory Animal Co., Ltd. without gender

distinction. VX2 tumor block was purchased from Shanghai lalan biotechnology co.,

LTD. Originally, the fresh tumor block was selected to prune to approximately 1 mm^3

size. After the rabbit had the anesthesia, the prepared 1 mm^3 size fresh tumor block was

sent to the liver with an 18-gauge trocar under ultrasound guidance. The 3.0T magnetic

resonance (Magnetom Skyra) was employed to diagnostic monitoring rabbit VX2 liver

tumor size on 21D after implantation of VX2 tumor block. Then, the VX2 liver tumor-

bearing rabbits were randomly divided into three groups (n=3): (1) ^{177}LuCl$_3$ (0.8 mL

per rabbit, ^{177}Lu: 29.60 MBq); (2) PCMs (0.8 mL per rabbit); (3) ^{177}Lu-PCMs (0.8 mL

per rabbit, containing 29.60 MBq for ^{177}Lu).

**In *vivo* intravascular brachytherapy and Imaging diagnostic monitoring for rat
liver tumor.** The procedure of N1S1 rat liver tumor model intervention was as follows.
After opening the abdominal cavity, the celiac, hepatic, and gastroduodenal arteries
were identified and carefully separated after anesthesia and laparotomy. Then, two
ligatures were placed around the gastroduodenal artery and the distal part of the
gastroduodenal artery was also ligated. A ligature was placed around the celiac artery
to temporarily interrupt blood flow. The gastroduodenal artery was punctured upstream
of the distal ligature using a self-made needle and then a catheter was placed into the

hepatic artery. After the administration of the drug (10 mg/mL, 200 μL), the proximal

part of the gastroduodenal artery (upstream of the puncture point) was tied off. The

ligature around the celiac artery was then removed and hepatic arterial flow was

restored. Rats bearing N1S1 liver tumors were divided into four groups (n=5 per group):

(1) saline control, (2) free $^{177}LuCl_3$ (14.80 MBq per rat), (3) PCMs, and (4) ^{177}Lu-PCM

groups (14.80 MBq per rat). Next, SPECT/CT imaging was performed at 2 h, 2 days, 5

days, and 10 days after treatment on the ^{177}Lu-PCM group. Subsequently, the evaluation

of the intervention was performed by nanoScan-SPECT/CT scanner and 9.4 T animal

MRI scanner. In addition, the tumor size was estimated by its largest (L) and smallest

(S) diameters using the following formula: Tumor volume $(mm^3) = (L \times S^2)/2$. All

animals were under mild anesthesia to obtain stable and accurate images. All rats were

euthanized on day 14. Hearts, normal liver, spleen, lung and kidney tissues, and tumors

in the liver were individually harvested. The samples were immediately immersed in 4%

paraformaldehyde and embedded in paraffin. Rat tissues were stained with H&E, and

imaging was conducted with the electron microscope. All histology samples were

analyzed by pathology researchers with 5 years of experience.

SPECT imaging study of Wistar rats was performed with a nanoScan-SPECT/CT

scanner (Mediso, Hungary).

In *vivo* intravascular brachytherapy and imaging diagnostic monitoring for rabbit

VX2 liver tumor model. $^{177}LuCl_3$, PCMs, or ^{177}Lu-PCMs was injected into the rabbit

VX2 liver tumor through TARE under the guidance of digital subtraction angiography

(DSA). Briefly, the VX2 liver tumor-bearing rabbits were anesthetized by intravenous

injection of 3% sodium pentobarbital (10-20 mg/kg) and the femoral artery was

separated to exposure. The microcatheter was sent to the artery through the vessel

sheath after the artery was punctured with an 18-gauge puncture needle. Then, under

the real-time guidance of DSA, a 2.1-F microcatheter and coaxial micro-guide wire

were inserted through the 5-F artery sheath selectively advanced into the blood supply

artery nearest to the tumor. Then, liver arteriography was performed to locate rabbit

VX2 liver tumors. Subsequently, $^{177}LuCl_3$ (29.6 MBq), PCMs, or ^{177}Lu-PCMs (^{177}Lu:

29.6 MBq) were manually pushed into the tumor through the microcatheter at a uniform and slow speed to avoid reflux. After administration, iohexol was injected to detect tumor vascular embolism in DSA subtraction mode, and images were collected. After withdrawing the microcatheter and suturing the wound, the antibiotic ampicillin (50,000-200,000 units/kg, twice daily) was injected intramuscularly into experimental rabbits 3 days after the operation to prevent wound infection and inflammation. Each VX2 liver tumor-bearing rabbit SPECT/CT (Siemens Symbia T16, Germany) imaging-guided scanning in a prone position after intravascular brachytherapy of 5 and 10 days to the measured distribution of ^{177}Lu in *vivo*. Meanwhile, the 3.0T magnetic resonance (Magnetom Skyra) with sequences of diffusion-weighted imaging (DWI), T2-weighted image (T2WI), apparent diffusion coefficient (ADC), and Gd contrast agent-enhanced T1-weighted image (T1WI-Gd) was employed to diagnostic monitoring rabbit liver VX2 tumor size after intravascular brachytherapy of 5 and 10 days. Subsequently, the liver VX2 tumor-bearing rabbits were euthanized after intravascular brachytherapy for 10 days and the samples of tumor tissues and peritumoral normal tissues were collected and fixed in 4.0% of paraformaldehyde in phosphate-buffered saline for preparation of tissue sections and H&E staining, and immunofluorescence staining with TUNEL, Ki-67, VEGF, and γ-H2AX, imaging was conducted with the electron microscope and fluorescence electron microscope, respectively. For the analysis of tumor cells or tumor-infiltrating T cells, tumor tissues were excised at the indicated time points, cut into small pieces, and placed in a dissociation buffer (1 mg ml^{-1} collagenase type IV and 0.1 mg ml^{-1} DNase I in RPMI) for 30 min at 37 °C with gentle shaking. The cell suspension was passed through a 70 μm strainer, washed with FACS buffer, and stained with the indicated antibodies or its isotype control, followed by flow cytometric analysis. The surface markers staining assays on tumor-infiltrating T cells were performed with fluorescent-labeled anti-CD3/CD8.

SPECT imaging study of rabbits and porcine was performed using a SPECT-CT scanner (Siemens Symbia T16, Germany).

Biological safety. After intravascular brachytherapy for 10 days, blood routine

examination including white blood cells (WBC), red blood cells (RBC), hemoglobin (HGB), and platelets (PLT) were tested with blood count apparatus. Peripheral blood was collected through the ear artery, and the glutamic oxalacetic transaminase (AST) and Alkaline phosphatase (ALP), albumin (ALB), alkaline phosphatase (ALP), and creatinine (CREA) were detected with the corresponding kit according to the operating instructions. Finally, after rabbits were euthanized, the major organs such as the heart, liver, spleen, lung, and kidney were collected for H&E staining.

In *vivo* IVIS fluorescence imaging. The IVIS images of excised rabbit VX2 liver tumor after DSA-guided embolization of Cy 5.5-labeled PCMs (10 mg/mL, 0.5 mL) for 5 days. The IVIS images were obtained 5 days post-embolization. Briefly, the VX2 liver tumor-bearing rabbits were anesthetized by intravenous injection of 3% sodium pentobarbital (10-20 mg/kg) and the femoral artery was separated to exposure. The microcatheter was sent to the artery through the vessel sheath after the artery was punctured with an 18-gauge puncture needle. Then, under the real-time guidance of DSA, a 2.1-F microcatheter and coaxial micro-guide wire were inserted through the 5-F artery sheath selectively advanced into the blood supply artery nearest to the tumor. Then, liver arteriography was performed to locate rabbit VX2 liver tumors. Subsequently, Cy 5.5-labeled PCMs (10 mg/mL, 0.5 mL) were manually pushed into the tumor through the microcatheter at a uniform and slow speed. The liver VX2 tumor-bearing rabbits were euthanized after 5 days and the samples of tumor tissues and the major organs such as the heart, liver, spleen, lung, and kidney were collected for IVIS fluorescence imaging to measure the biodistribution of PCMs in vivo and monitoring for pulmonary shunts.

***Ex vivo* anti-tumor effects and SPECT/CT imaging.** All procedures involving human participants were following the ethical standards of the institution. The study was approved by the Institutional Review Board of Affiliated Hospital of Southwest Medical University (IRB No. KY2022154). The subjects signed and gave written informed consent. We collected and kept 10 consecutive freshly resected liver tumors in the medium. Within 2 hours of harvesting, these tumors were injected with ^{177}Lu-

PCMs (74.0 MBq). Tumor tissues were photographed, and SPECT/CT images were obtained 0 and 3 days after injection. Treated tissues were partially submerged in a medium and then incubated inside a humidified container at 37°C for 3 days. SPECT/CT imaging was repeated at 3 days after ^{177}Lu-PCMs injection, followed by fixation in 10% buffered formalin and histologic processing to generate paraffin-embedded tissue sections[38].

Statistical Analysis. All the results in this work were presented as mean values ± SD. Statistical analyses were performed with GraphPad Prism 8.3 software. Statistical significances were calculated via Student's t-test or Mann−Whitney U test. $*p < 0.05$, $**p < 0.01$, and $***p < 0.001$.

References

1. Chargari C*, et al.* Brachytherapy: An overview for clinicians. *CA-Cancer J. Clin.* **69**, 386-401 (2019).

2. Forner A, Gilabert M, Bruix J, Raoul J-L. Treatment of intermediate-stage hepatocellular carcinoma. *Nat. Rev. Clin. Oncol.* **11**, 525-535 (2014).

3. Mumper R.J., Yun Ryo U, Jay M. Neutron-activated holmium-166-Poly (L-hactic acid) microspheres: A potential agent for the internal radiation therapy of hepatic tumors. *J. Nucl. Med.* **32**, 2139 (1991).

4. Wondergem M*, et al.* ^{99m}Tc-macroaggregated albumin poorly predicts the intrahepatic distribution of ^{90}Y resin microspheres in hepatic radioembolization. *J. Nucl. Med.* **54**, 1294 (2013).

5. Cvjetinović Đ*, et al.* Bioevaluation of glucose-modified liposomes as a potential drug delivery system for cancer treatment using 177-Lu radiotracking. *J. Control. Release.* **332**, 301-311 (2021).

6. Rahbar K*, et al.* German multicenter study investigating ^{177}Lu-PSMA-617 radioligand therapy in advanced prostate cancer patients. *J. Nucl. Med.* **58**, 85 (2017).

7. Jing L*, et al.* ^{177}Lu-Labeled cerasomes encapsulating indocyanine green for cancer theranostics. *ACS Appl. Mater. Inter.* **7**, 22095-22105 (2015).

8. Price E.W., Orvig C. Matching chelators to radiometals for radiopharmaceuticals.

Chem. Soc. Rev. **43**, 260-290 (2014).

9. Pellico J, Gawne P.J., R TMdR. Radiolabelling of nanomaterials for medical imaging and therapy. *Chem. Soc. Rev.* **50**, 3355-3423 (2021).

10. Li J*, et al.* Site-specific allylic C–H bond functionalization with a copper-bound N-centred radical. *Nature* **574**, 516-521 (2019).

11. Xu N*, et al.* γ-Ray-sensitive motif-driven versatile epoxy thermoset: Highly efficient radiation degradation, intrinsic flame resistance and sustainable synthesis. *Chem. Eng. J.* **450**, 138151 (2022).

12. Herrerías CI, Yao X, Li Z, Li C-J. Reactions of C−H Bonds in Water. *Chem. Rev.* **107**, 2546-2562 (2007).

13. Han G, Liu J.T., Lu K.J., Chung T-S. Advanced anti-fouling membranes for osmotic power generation from wastewater via pressure retarded osmosis (PRO). *Environ. Sci. Technol.* **52**, 6686-6694 (2018).

14. Marignier J.L., Belloni J, Delcourt M.O., Chevalier J.P. Microaggregates of non-noble metals and bimetallic alloys prepared by radiation-induced reduction. *Nature* **317**, 344-345 (1985).

15. Thanoo B.C., Sunny M.C., Jayakrisnnan A. Tantalum-loaded polyurethane microspheres for particulate embolization: preparation and properties. *Biomaterials* **12**, 525-528 (1991).

16. Biquard X, Víllora EG, Shimamura K, Lorenz K. XANES/EXAFS study of the Lu and Y incorporation in the single crystal $Tb_3Sc_2Al_3O_{12}$ Faraday rotator. *J. Appl. Phys.* **127**, 115106 (2020).

17. Lu T, Chen Q. Independent gradient model based on Hirshfeld partition: A new method for visual study of interactions in chemical systems. *J. Comput. Chem.* **43**, 539-555 (2022).

18. Lu Y, Wang Y, Chen J. Adjustable capillary imbibition enhancement in double-walled nanotubes with concentric tube length difference. *J. Stat. Mech-Theory. E.* **2021**, 053204 (2021).

19. Hummer G, Rasaiah J.C., Noworyta J.P. Water conduction through the hydrophobic channel of a carbon nanotube. *Nature* **414**, 188 (2001).

20. Humphrey W, Dalke A, Schulten K. VMD: Visual molecular dynamics. *J. Mol. Graph.* **14**, 33-38 (1996).

21. Narsinh K.H.*, et al.* Hepatopulmonary shunting: A prognostic indicator of survival in patients with metastatic colorectal adenocarcinoma treated with ^{90}Y radioembolization. *Radiology* **282**, 281-288 (2016).

22. Dudev T, Lim C. Competition among metal ions for protein binding sites: determinants of metal ion selectivity in proteins. *Chem. Rev.* **114**, 538-556 (2014).

23. O'Neill E*, et al.* Imaging DNA damage repair in vivo after ^{177}Lu-DOTATATE therapy. *J. Nucl. Med.* **61**, 743 (2020).

24. Chew V*, et al.* Immune activation underlies a sustained clinical response to Yttrium-90 radioembolisation in hepatocellular carcinoma. *GUT* **68**, 335-346 (2019).

25. Elschot M*, et al.* ([99]m)Tc-MAA overestimates the absorbed dose to the lungs in radioembolization: a quantitative evaluation in patients treated with [166]Ho-microspheres. *Eur. j. nucl. med. mol. i.* **41**, 1965-1975 (2014).

26. Smits MLJ*, et al.* The superior predictive value of [166]Ho-scout compared with ([99]m)Tc-macroaggregated albumin prior to [166]Ho-microspheres radioembolization in patients with liver metastases. *Eur. j. nucl. med. mol. i.* **47**, 798-806 (2020).

27. Zhao Y, Truhlar D.G. The M06 suite of density functionals for main group thermochemistry, thermochemical kinetics, noncovalent interactions, excited states, and transition elements: two new functionals and systematic testing of four M06-class functionals and 12 other functionals. *Theor. Chem. Acc.* **120**, 215-241 (2007).

28. Hehre W.J., Ditchfield R, Pople J.A. Self—consistent molecular orbital methods. XII. further extensions of gaussian—type basis sets for use in molecular orbital studies of organic molecules. *J. Chem. Phys.* **56**, 2257-2261 (1972).

29. Ravel B, Newville M. ATHENA, ARTEMIS, HEPHAESTUS: data analysis for X-ray absorption spectroscopy using IFEFFIT. *J. Synchrotron. Radiat.* **12**, 537-541 (2005).

30. Rehr J.J., Kas J.J., Vila F.D., Prange M.P., Jorissen K. Parameter-free calculations of X-ray spectra with FEFF9. *Phys. Chem. Chem. Phys.* **12**, 5503-5513 (2010).

31. Frisch M*, et al.* Gaussian 09 (Gaussian, Inc., Wallingford, CT, 2009). (2005).

32. Lee C, Yang W, Parr R.G. Development of the Colle-Salvetti correlation-energy formula into a functional of the electron density. *Phys. Rev. B.* **37**, 785-789 (1988).

33. Lu T, Chen F. Multiwfn: A multifunctional wavefunction analyzer. *J. Comput. Chem.* **33**, 580-592 (2012).

34. Plimpton S. Fast parallel algorithms for short-range molecular dynamics. *J. Comput. phys.* **117**, 1-19 (1995).

35. Picallo C.B., Gravelle S, Joly L, Charlaix E, Bocquet L. Nanofluidic osmotic diodes: theory and molecular dynamics simulations. *Phys. Rev. Lett.* **111**, 244501 (2013).

36. Chen J. Phonon-induced ratchet motion of a water nanodroplet on a supported black phosphorene. *J. Phys. Chem. Letter.* **11**, 4298-4304 (2020).

37. Rappe A.K., Casewit C.J., Colwell K.S., Goddard W.A., Skiff W.M. UFF, a full periodic table force field for molecular mechanics and molecular dynamics simulations. *J. Am. Chem. Soc.* **114**, 10024-10035 (1992).

38. PCNA SH. Percutaneous liquid ablation agent for tumor treatment and drug delivery. *Sci. Transl. Med.* **13**, (2021).

Acknowledgements

Author contributions

X.X., H.M., and G.L. conceived the project. X.X., H.Chen, Y.W., P.H., Z.Z., H.Cheng, X.G., Y.S., B.L. and C.L. performed the experiments and analysed the results. Y.L., J.H. and Y.P. performed the SPECT/CT test, X.X. and Y.W. assisted with the EXAFS analysis. J.M., H.Chen, and Y.Z. performed the DSA-guide for IAB experiments. X.X., G.L., H.C., C.C., and H.M. wrote the manuscript. G.L. supervised the entire project. All authors discussed the results and edited on the manuscript.

Competing interests

G.L., H.M., and X.X. are inventors on a patent (ZL113018463B) related to this study. The other authors declare no competing interests.

Data availability

The authors declare that data supporting the findings of this study are available within the article and its Supplementary Information files. All relevant data can be provided by the authors upon reasonable request.

Supplementary Files

This is a list of supplementary files associated with this preprint. Click to download.

- SupplementaryMaterials.pdf